JGR Earth Surface

RESEARCH ARTICLE
10.1029/2020JF005860

Modeled and Observed Bedrock Displacements in North-East Greenland Using Refined Estimates of Present-Day Ice-Mass Changes and Densified GNSS Measurements

Maria T. Kappelsberger[1], Undine Strößenreuther[1], Mirko Scheinert[1], Martin Horwath[1], Andreas Groh[1], Christoph Knöfel[1], Susanne Lunz[1,2], and Shfaqat A. Khan[3]

[1]Institut für Planetare Geodäsie, Technische Universität Dresden, Dresden, Germany, [2]GFZ German Research Centre for Geosciences, Potsdam, Germany, [3]Department of Geodesy and Earth Observations, DTU Space, National Space Institute, Technical University of Denmark, Lyngby, Denmark

Key Points:

- Geodetic Global Navigation Satellite System (GNSS) measurements at bedrock sites in north-east Greenland revealed uplift rates in the range of 2.8 to 8.9 mm yr^{-1}
- Elastic predictions were derived from ice-mass change estimates combining Gravity Recovery and Climate Experiment and CryoSat-2 data and including peripheral glaciers
- Models predicting low glacial-isostatic adjustment rates (0.7–4.4 mm yr^{-1} at the GNSS sites) were confirmed

Supporting Information:

- Supporting Information S1

Correspondence to:
M. T. Kappelsberger,
maria.kappelsberger@tu-dresden.de

Citation:
Kappelsberger, M. T., Strößenreuther, U., Scheinert, M., Horwath, M., Groh, A., Knöfel, C., et al. (2021). Modeled and observed bedrock displacements in north-east Greenland using refined estimates of present-day ice-mass changes and densified GNSS measurements. *Journal of Geophysical Research: Earth Surface*, *126*, e2020JF005860. https://doi.org/10.1029/2020JF005860

Received 26 AUG 2020
Accepted 6 JAN 2021

Abstract Models of the glacial-isostatic adjustment (GIA) to past ice-mass changes exhibit large differences in north-east Greenland owing to insufficient knowledge about glacial history and Earth rheology. The GIA uncertainties feed back to uncertainties in present-day mass-balance estimates from satellite gravimetry. Geodetic Global Navigation Satellite System (GNSS) measurements allow to directly observe displacement of bedrock. We present results from repeated and continuous GNSS measurements conducted within five measurement campaigns between 2008 and 2017. We used the observed uplift rates to validate different GIA models in conjunction with estimates of the elastic response of the solid Earth to present-day ice-mass changes. To determine present-day ice-mass changes and the associated elastic deformations, we combined satellite altimetry data from CryoSat-2 with satellite gravimetry data from the Gravity Recovery and Climate Experiment for the entire Greenland Ice Sheet (GrIS) and included peripheral glaciers and ice caps. The different GIA models were consistently used in all processing steps. The GNSS measurements in north-east Greenland revealed uplift rates in the range of 2.8 to 8.9 mm yr^{-1}. The comparison of the total displacement predicted by GIA and elastic modeling with the GNSS-based displacement clearly favors GIA models that show low rates (0.7–4.4 mm yr^{-1} at the GNSS sites) against GIA models with higher rates of up to 8.3 mm yr^{-1}. The correction due to the favored GIA model in north-east Greenland results in an ice-mass loss of 233 ± 43 Gt yr^{-1} for the GrIS including peripheral glaciers over the period July 2010 to June 2017.

1. Introduction

Over the last decades the Greenland Ice Sheet (GrIS) has undergone a substantial shrinking of its mass. The mass loss is dominated by an accelerating discharge of outlet glaciers in south-east, west, and north-west Greenland (Khan et al., 2015). After glaciers in north-east Greenland had a longer period of relative stability they have shown an increase in dynamic thinning (Khan et al., 2014) and surface melt water runoff (Noël et al., 2019) since the early 2000s. To deal with this area in detail one has to take a closer look at the North-East Greenland Ice Stream (NEGIS). Accounting for about 16% of the entire area of the ice sheet (Khan et al., 2014), NEGIS originates near the summit and splits into the three main branches, Nioghalvfjerdsbræ (NG), Zachariae Isstrøm (ZI), and Storstrømmen (SN) (Figure 1). At present, the mass loss of the GrIS equals about 0.7 mm yr^{-1} of global sea-level rise (Forsberg et al., 2017; Shepherd et al., 2019; WCRP Global Sea Level Budget Group, 2018). The share of NG and ZI contribute less than 5% to this rise (Mouginot et al., 2019). However, in the consequence of ocean warming (Schaffer et al., 2020) the front of ZI will likely retreat another 30 km over the next decades and if, moreover, frontal melt rates exceed 6 m d^{-1}, ZI alone might contribute 16 mm to global mean sea level by 2,100 (Choi et al., 2017). Hence, it is essential to monitor ice-surface elevation and mass balance in order to detect and understand any substantial changes.

Three main approaches are commonly used in order to infer the mass balance of ice sheets, namely the mass-budget method, the gravity-change approach and the altimetry method. Results of the three methods were recently intercompared by Shepherd et al. (2019) and Bamber et al. (2018). However, the majority of previous studies applied each method separately (e.g., for satellite altimetry: Hurkmans et al., 2014; McMillan

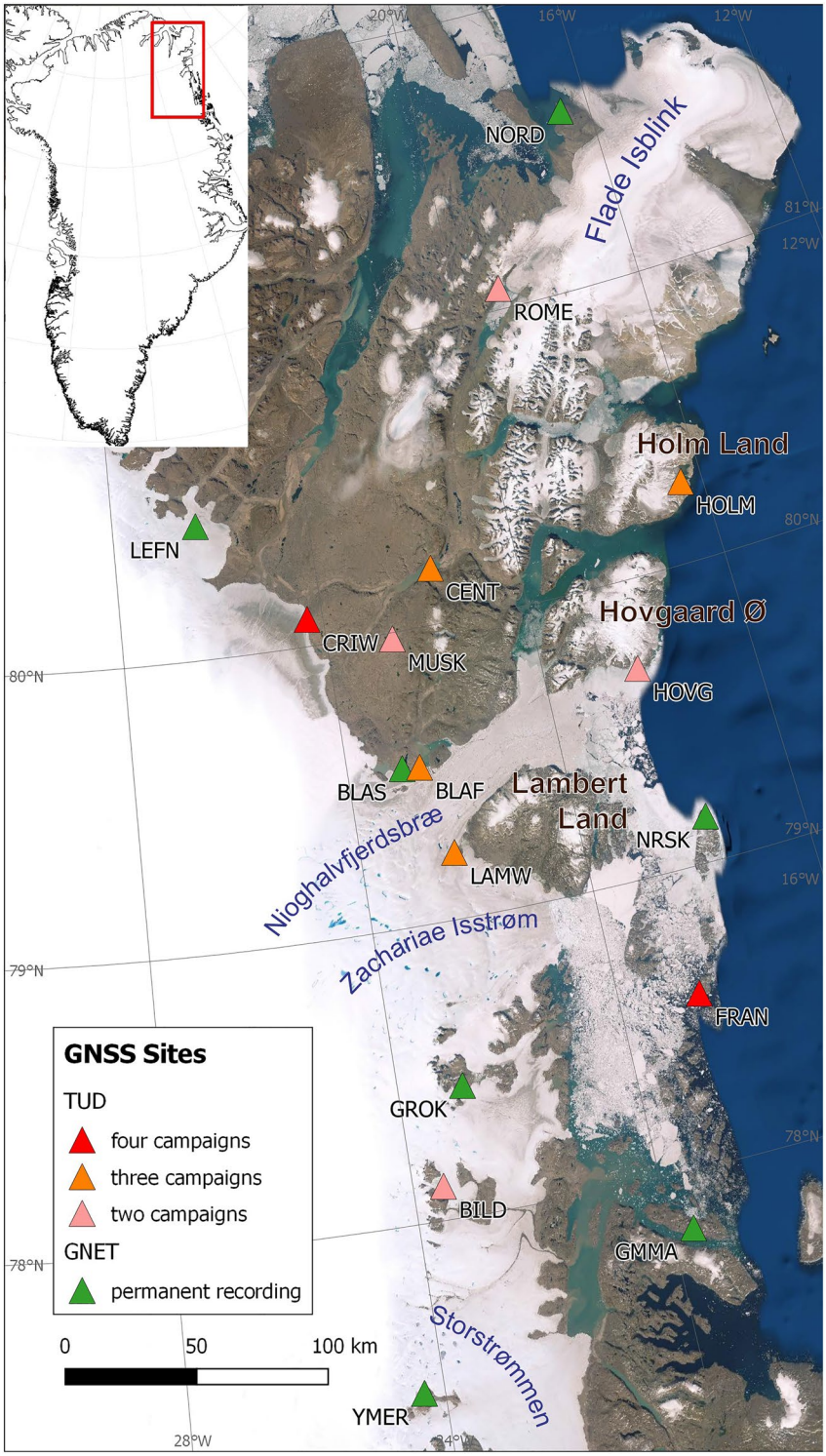

Figure 1. Map of the study area. The main outlet glaciers, Nioghalvfjerdsbræ (NG), Zachariae Isstrøm (ZI) and Storstrømmen (SN), the ice caps Flade Isblink and Holm Land, the islands Hovgaard Ø and Lambert Land are shown (geographical names after Weidick, 1995). TUD GNSS (with the measured number of campaigns) and GNET sites are indicated by different colored triangles. GNET, Greenland GPS network; GNSS, Global Navigation Satellite System; TUD, Technische Universität Dresden.

et al., 2016; Sørensen et al., 2011; e.g., for satellite gravimetry: Groh et al., 2019; Luthcke et al., 2006; Mottram et al., 2019; Schrama et al., 2014; Wouters et al., 2008).

The mass-balance estimation by satellite gravimetry is hampered as it depends on glacial-isostatic adjustment (GIA) correction. GIA describes the response of the solid Earth to changing ice load throughout the glacial history. This process involves a viscous mass flow in the Earth interior, mainly in the asthenosphere. Resulting effects, which are observable by geodetic methods, comprise a deformation of the Earth surface and a change of the geoid. Thus, altimetric and gravimetric mass-balance estimates have to be corrected for the GIA effect. However, estimates from gravimetry are more affected by the GIA correction and its uncertainty than estimates from altimetry, because the contribution of the GIA-induced solid Earth deformation to the total observed altimetric height change is small in contrast to the contribution of the GIA-induced mass-equivalent change to the total observed gravimetric mass change (Gunter et al., 2014; Wahr et al., 2000). For Greenland, Shepherd et al. (2019) reported a spread of the mass-equivalent GIA effect from −27 to 21 Gt yr^{-1} predicted by six different GIA models. Wake et al. (2016) ascribed an average uncertainty of about 26 Gt yr^{-1} to the GIA prediction mainly due to the insufficient knowledge of the rheological properties of the Earth. This means that for the GrIS as a whole the GIA-related uncertainty is in the order of 10% of the mass loss signal (Wake et al., 2016). For individual drainage basins, however, the GIA contribution and its uncertainty can be significantly larger in relation to the ice-mass change. Especially in north-east Greenland the mass-change rate and the GIA signal might have similar magnitudes (Barletta et al., 2013).

The mass-balance estimation by satellite altimetry is complicated as it requires assumptions about the firn structure in order to convert the altimetric height measurements to mass, whereas satellite gravimetry is directly sensitive to mass redistributions. In contrast to satellite gravimetry, however, altimetry data can be used to determine mass changes at a higher spatial resolution. Exploiting the synergy of the two satellite techniques improves ice-mass change estimates (Forsberg et al., 2017; Sasgen et al., 2019). This requires a consistent treatment of the different satellite-based data sets together with the GIA effect. In addition, the contribution of peripheral glaciers and ice caps to the Greenland mass loss cannot be neglected (Bolch et al., 2013; Gardner et al., 2013; Marzeion et al., 2012). Combination approaches for Greenland using data from the Gravity Recovery and Climate Experiment (GRACE) and various satellite altimetry missions were recently published by Colgan et al. (2015) and Forsberg et al. (2017). Whereas Colgan et al. (2015) incorporated peripheral glaciers according to the Greenland glacier inventory (Citterio & Ahlstrøm, 2013), Forsberg et al. (2017) included them to a variable extent adapted to the availability of altimetry data. Both performed their combination analysis on a spatial grid resolution of about 25 × 25 km^2 and accounted for the GIA signal using the model ICE-5G (Peltier, 2004).

In addition to the long-term GIA deformation, contemporary ice-mass changes cause an immediate deformation ascribed to the elastic properties of the Earth. The total deformation can be directly observed by precise geodetic Global Navigation Satellite System (GNSS) measurements (King et al., 2010). L. Wang et al. (2019) used measurements of the Greenland Global Positioning System (GPS) network (GNET) to evaluate predicted elastic displacement rates. The predicted rates were derived from GRACE (GIA-corrected using the model from A et al., 2013) at a spatial grid resolution of 0.5° × 0.5°. They were scaled by factors empirically inferred from surface mass balance (SMB) and altimetric surface-elevation change data in order to compensate for GRACE's coarse spatial resolution. The predicted rates were then compared to the GNET-observed rates which were GIA-corrected using the model from Khan et al. (2016). Nevertheless, L. Wang et al. (2019) noted that the predicted elastic response for GNSS sites near concentrated ice-mass changes was underestimated. Furthermore, they discussed whether discrepancies between GRACE and GNSS uplift rates might have arisen from an inconsistent treatment of the GIA correction.

With this study we present the results of repeated GNSS measurements in north-east Greenland carried out in 2008, 2009, 2016, and 2017. Since the site selection was well-coordinated with GNET it is possible to infer vertical displacement rates with a denser coverage as well as to mutually verify the results. We aim at using the GNSS-inferred rates as independent observations of solid Earth surface displacement to validate predicted displacement rates inferred from a combination of satellite methods and GIA model predictions. For this, we combine satellite gravimetry (GRACE) with satellite altimetry (CryoSat-2) data to solve for refined present-day ice-mass changes. We use this refined solution to derive an improved prediction of elastic deformation rates. A grid resolution of 1.5 × 1.5 km^2 adopted for north-east Greenland enables to resolve changes

at the glacier scale. However, the combination approach is not restricted to the study area. It is implemented for the entire GrIS including the contribution of peripheral glaciers. In this way, we account for the spatially integrative nature of GRACE solutions. Greenland-wide ice-load variations are also needed to predict the elastic response in north-east Greenland. Whenever GIA model predictions are implied in the data processing they are used consistently. The total bedrock displacement, calculated as the sum of modeled GIA-induced vertical displacement rate and the refined elastic rate, is compared against the independent GNSS results. This finally enables us to evaluate estimates of gravimetric ice-mass changes and to narrow the range of GIA corrections at least for north-east Greenland where the GNSS measurements are available.

2. Ice-Mass Changes and GIA in North-East Greenland

The two northern branches of NEGIS, Nioghalvfjerdsbræ (NG) and Zachariae Isstrøm (ZI), are marine-terminating glaciers and subject to a complex interaction with the ocean. Calving at and shrinking of their floating ice tongues are related to increasing temperature of both air and sea surface (Khan et al., 2014; Mouginot et al., 2015). Furthermore, the submarine melting of NG's ice shelf is driven by warmer water inflow of North Atlantic origin that finds a direct subsurface pathway through a trough system on the continental shelf (Schaffer et al., 2020, 2017). It is presumed that the ocean heat is also transported to the cavity of ZI (Schaffer et al., 2020). Since 2002, the ice front of ZI has retreated and by 2014, ZI transformed into a tidewater glacier with a grounded terminus (Mouginot et al., 2015). In contrast, NG still keeps a buttressing ice tongue although it thinned by 26% from 1998 to 2014 (Mayer et al., 2018). As a response to the decreasing thickness of their floating ice tongues NG's and ZI's grounding lines migrated inland (Mouginot et al., 2015). The grounding line of NG gradually moved back on a prograde bed from 1992 to 2011 and remained stable since (Mouginot et al., 2015). The grounding line of ZI has retreated rapidly on a retrograde bed since 1996 (Mouginot et al., 2015). Contrasting developments of NG and ZI were also identified by Krieger, Strößenreuther et al. (2020) from CryoSat-2 and TanDEM-X data over the period 2011–2014. For the drainage basin of ZI they observed a mass loss more than three times larger than for NG (3.6 ± 1.2 vs. 1.0 ± 1.0 Gt yr^{-1}). In contrast, Mouginot et al. (2019), by applying the mass-budget method, estimated a mean mass loss of about 3 Gt yr^{-1} for each of the two glacier catchment areas (ZI: 3.0 ± 0.4 Gt yr^{-1}, NG: 3.5 ± 0.2 Gt yr^{-1}) over the period 2010–2017.

NEGIS' southern branch, Storstrømmen (SN), forms the third largest drainage basin after NG and ZI. SN is a surge-type glacier whose surge cycle is characterized by long active phases with a slow surge initiation and termination (Mouginot et al., 2018). During the surge, subglacial water pressure causes rapid basal sliding and, therefore, a large advance of terminus positions. Mouginot et al. (2018) suggested that basal pressure at the bed of SN was enhanced due to subglacial melt water coming from the upper NEGIS. The melt water could accumulate at the bed of SN since its topography is characterized by a deep basin upstream the grounding line. The last active phase of SN took place from 1978 to 1988. Since then, the glacier has been in a quiescent phase with ice thickening in the upper part and thinning in the lower part (Mouginot et al., 2018). Over the period 2010–2017 Mouginot et al. (2019) reported a mean mass loss of 0.5 ± 0.1 Gt yr^{-1}.

Greenland's largest ice cap Flade Isblink is located in the far north-east of our study area. Rinne et al. (2011) determined its surface-elevation changes from Envisat radar altimetry and ICESat laser altimetry for the period 2004–2008. Both altimeter missions revealed the same pattern: elevation increased in the north-west (probably driven by ice dynamics of surge-type glaciers) and decreased in the south-east (probably due to SMB). According to Rinne et al. (2011) and Gardner et al. (2013), the mean surface-elevation change and mass-change rate of Flade Isblink was close to zero.

Ice mass changes since the Last Glacial Maximum dominate the GIA signal. Thus, besides a model of the Earth's rheology, modeling GIA has to incorporate reconstructions of the glacial history. For north-east Greenland such reconstructions show an equivocal picture. This applies to the expansion of the GrIS during the Last Glacial Maximum and its evolution since that time, which has been dominated by mass loss. Detailed studies on the entire ice sheet were published by, for example, Funder and Hansen (1996), Le Meur and Huybrechts (1998), Tarasov and Peltier (2002), Fleming and Lambeck (2004), Simpson

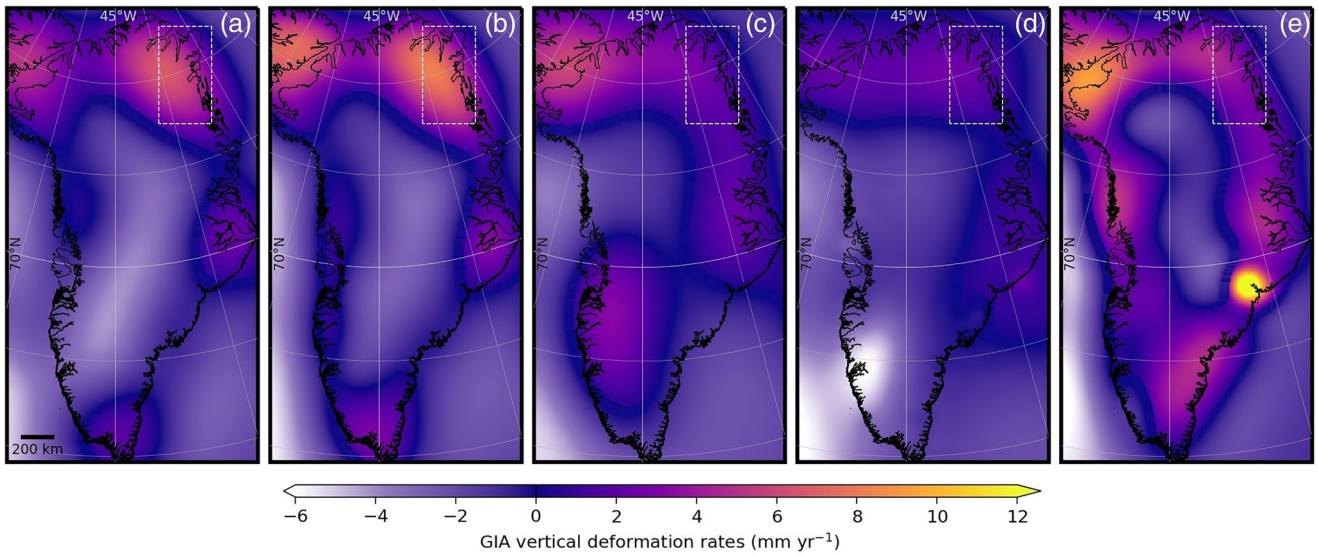

Figure 2. Vertical displacement rates predicted by the GIA models considered in this study: (a) A13 (A et al., 2013), (b) ICE-6G_D (VM5a) (Peltier et al., 2015, 2018), (c) Caron (Caron et al., 2018), (d) Huy3 (Lecavalier et al., 2014), and (e) GNET-GIA (Khan et al., 2016). The white box indicates the study area in north-east Greenland. Here and in all following figures longitude and latitude gridlines are shown every 15° and 5°, respectively. GIA, glacial-isostatic adjustment; GNET, Greenland GPS network.

et al. (2009), Lecavalier et al. (2014), and on north-east Greenland by, for example, Weidick et al. (1996), Evans et al. (2009), Wagner and Bennike (2014), Larsen et al. (2018), Strunk et al. (2018).

In this study, we investigate three global GIA models, namely A13 (A et al., 2013), ICE-6G_D (VM5a) (Peltier et al., 2015, 2018) (abbreviated as ICE-6G below), and Caron (Caron et al., 2018). In addition, we investigate two GIA models constructed for the region of Greenland, namely Huy3 (Lecavalier et al., 2014) and GNET-GIA (Khan et al., 2016). All these models assume a spherically symmetric, gravitationally self-consistent Earth and the density and elastic Earth structure based on the preliminary reference Earth model (PREM) (Dziewonski & Anderson, 1981). They assume a purely elastic lithosphere and model the mantle rheology as a linear Maxwell material. All models except GNET-GIA use compressible Earth models. The choice of compressible versus incompressible Earth models has an insignificant effect on vertical displacement rates as long as the elastic response to present-day load changes is not included (Tanaka et al., 2011). The models differ in terms of the applied ice-load history, the assumed viscosity profile, and whether in-situ data in Greenland were used as constraints or not. In the following, we summarize these aspects for each model.

A et al. (2013) (Figure 2a) adopted the global ice-load history ICE-5G (Peltier, 2004) and the multilayered viscosity profile VM2 (Peltier, 2004). In ICE-5G, constraints for Greenland's glacial history are given by 16 relative sea-level (RSL) observations and numerical models of ice mechanics (Tarasov & Peltier, 2002). The model is able to reproduce the vertical displacement rates of the three available GNSS sites in Greenland. However, no GNSS station and only one RSL record is located in our study area (Tarasov & Peltier, 2002).

The refinement of ICE-5G to ICE-6G (Figure 2b) consisted mainly in using GNSS constraints from about 1,000 global sites (Peltier et al., 2015). While the Greenland component of the model was not modified, the ice-load history of North America, Antarctica, and north-west Eurasia was adjusted to the GNSS observations. The applied viscosity profile VM5a forms a five-layer fit to the prior VM2 model.

The Caron model (Figure 2c) represents the mean of an ensemble of 128,000 forward models calculated in a Bayesian framework. Caron et al. (2018) varied, for each model run, the combination of rheological parameters (effective elastic thickness of the lithosphere, upper mantle viscosity, lower mantle viscosity) and scaling coefficients for the ice-load history of the Australian National University (ANU) model (Lambeck et al., 2010, 2014). The probability of each model was computed by its comparison to 11,451 RSL and 459 GNSS records where the GNSS stations were confined to Europe, North America, and Antarctica. The

final GIA signal followed from a weighting of the individual GIA solutions inferred by the probabilistic information.

The regional GIA model Huy3 (Lecavalier et al., 2014) (Figure 2d) builds upon the model Huy2 (Simpson et al., 2009) by considering a larger data set of Greenland-wide RSL changes and past ice extent data. The Greenland ice-load history is simulated by the glaciological model as described by Huybrechts (2002). In order to account for the influence of the deglaciation of the North American ice sheet Lecavalier et al. (2014) adopted glaciological reconstructions from Tarasov et al. (2012). Outside of Greenland and North America, ICE-5G (Peltier, 2004) represents the background global ice-load history. Different Earth viscosity models, characterized by the effective elastic thickness of the lithosphere and the viscosities of the upper and lower mantle, were investigated in order to find the optimal model fit for each ice model reconstruction applying the GIA modeling jointly with solving the sea-level equation and accounting for GIA-induced Earth rotation perturbations.

For the regional model GNET-GIA (Figure 2e) Khan et al. (2016) adopted a scaled version of the local ice-load history Green1 (Fleming & Lambeck, 2004) and, outside of Greenland, the global ANU ice-load history model. Scaling factors were determined for each of Greenland's drainage basins individually by adjusting the modeled GIA rates to GNSS-measured uplift rates from GNET corrected for elastic loading (Bevis et al., 2012). In regions with a high density of RSL constraints, including north-east Greenland, scaling factors were close to one. Khan et al. (2016) used their viscosity profile VM-GPS for each basin, except for a small catchment area in south-east Greenland. This region is expected to be characterized by the Iceland hot spot track, therefore a thinner lithosphere and a low-viscosity asthenosphere were assumed.

The vertical displacement pattern predicted by these five GIA models show large discrepancies in north-east Greenland (Figure 2): lowest maximum rates revealed by Huy3 (2.7 mm yr^{-1}) and Caron (3.2 mm yr^{-1}), followed by GNET-GIA (4.9 mm yr^{-1}) and A13 (6.8 mm yr^{-1}), whereas ICE-6G yields the highest maximum rate (8.3 mm yr^{-1}).

3. Geodetic Data

3.1. Vertical Displacement Rates From Geodetic GNSS Measurements

We determined the bedrock displacements using geodetic GNSS measurements. For this purpose, in 2008 and 2009 we established more than 20 geodetic GNSS sites in the ice-free coastal region of north-east Greenland between 72°N and 81°N. For the realization of a long-term and stable monumentation we used special bolts that were directly fixed into bedrock. This allows a precise reoccupation and forced centering of the GNSS antennas when carrying out repeated observations. Thus, systematic effects could be minimized when using the same individual GNSS antenna at each site. The site locations were chosen in close coordination with the GNET of permanently recording stations. Our Technische Universität Dresden (TUD) network of campaign style sites and the GNET network of permanently recording sites complement each other by improving the coverage (Figure 1) but also enabling cross-checkings. In this region, the GNET sites were also set up in 2008 and 2009 (Khan et al., 2016). For this study we could make use of 10 sites north of 78°N which were observed for the first time in 2008 and 2009, and were remeasured in 2016 and 2017 (Figure 1). In this way, we obtained three or four measurement epochs for six sites, and two epochs for four sites, spanning a time period of 8–9 years.

The analysis was performed according to the differential approach (DGNSS) using the Bernese GNSS Software (Dach et al., 2015). The observational data of six GNET sites situated in the working area were analyzed jointly with the data of the TUD observation campaigns. For this, the GNET sites were treated as campaign sites by using subsets of the time series corresponding to the TUD campaign intervals. This allows to compare our results with those of the time series analysis by Khan et al. (2016). For the processing, precise data have to be introduced such as for satellite orbits, clocks, and Earth rotation parameters (Dach et al., 2020). Further models and auxiliary data were used to correct for additional effects, among others antenna phase center variations, tropospheric refraction (Boehm et al., 2006), higher-order ionospheric propagation delay (Fritsche et al., 2005), solid-Earth tides, pole tides, ocean tidal loading, tidal and nontidal atmospheric loading. Thereby the conventions of the International Earth Rotation and Reference Systems Service were taken into account (Petit & Luzum, 2010). The reference frame was realized by including seven

sites of the International GNSS Service (IGS) (four of them in Greenland), adopting the GNSS-only solution of the ITRF2014, IGS14 (Altamimi et al., 2016; Rebischung et al., 2016). With regard to the origin the center of mass of the entire Earth system (CM) was adopted.

The final network solution was adjusted using constraints to minimize no-net-rotation and no-net-translation toward the IGS sites. The final solution comprises three-dimensional (3D) coordinates referred to the epoch January 1, 2010 (same epoch as IGS14/ITRF2014) and linear 3D velocities for each site.

A realistic estimation of the obtained accuracy has to be based on a time series analysis taking correlations between the measurements into account which is done by incorporating models for colored (flicker) noise (Williams, 2003). Respective software solutions adopt such noise models and perform a robust trend estimation (Blewitt et al., 2016; Williams, 2008). In the case of campaign style GNSS measurements such a thorough time series analysis cannot be performed. Instead, we used the residuals r_i of a seven-parameter Helmert transform of the daily coordinate solutions with reference to the total coordinate solution in terms of the north, east, and vertical components. The variance of the mean daily solution was computed by

$$\sigma^2 = \frac{\sum r_i^2}{d(d-1)} \tag{1}$$

where d is the number of days. To account for the time-dependent correlations (colored noise) the standard deviation was scaled by an empirical factor $f = 3$ for the horizontal components, and $f = 5$ for the vertical component (Rülke, 2009):

$$\bar{\sigma} = f \cdot \sigma. \tag{2}$$

Thus, $\bar{\sigma}$ is a measure for the daily repeatability of the coordinate solutions. To estimate the accuracy of the inferred velocities, by variance propagation we find

$$\sigma_v^2 = \frac{2 \cdot \bar{\sigma}}{y^2} \tag{3}$$

where y is the maximum time span (in years) between the observation epochs at the respective site. However, to come up with a realistic uncertainty measure further effects have to be taken into account such as the uncertainties of the reference frame realization and of the various models used in the processing. Furthermore, Bevis et al. (2012) investigated the impact of seasonal ice-load changes and atmospheric changes on the velocities inferred for the GNET sites. While we account for atmospheric effects (see above), the effect of the seasonal cycle of ice-mass changes is minimized to the greatest possible extent since the campaign style GNSS measurements mostly took place at the same time of the year. Moreover, the measurements cover a long time span of 8 to 9 years with (in most cases) more than two observation epochs. Therefore, we assume that seasonal effects are canceled out or are, at least, minimized. Nevertheless, in order to account for all these remaining uncertainties, an additional variance is added, and the final variance of the inferred velocities is calculated by variance propagation

$$\bar{\sigma}_v^2 = \sigma_v^2 + \sigma_{\text{rem}}^2 \tag{4}$$

where $\sigma_{\text{rem}}^2 = 1$ mm yr^{-1} for the north and east components, and $\sigma_{\text{rem}}^2 = 1.5$ mm yr^{-1} for the vertical (up) component.

The resulting uplift rates together with their uncertainty measures are given in Table 1. Note that the GNET data were also treated as campaign style observations to facilitate a consistent processing. As their end time the epoch of the last TUD campaign-style observations was chosen (Table 1, site FRAN Franske Øer). Even more, in this way it is possible to validate the results obtained at the campaign sites by comparing with the GNET results (a) in terms of the campaign style processing and (b) given by Khan et al. (2016) for the time series analysis (Table S1). Since no GNET data from the station NORD were available at the time of the GNSS analysis, we refer to the results of Khan et al. (2016) in the following investigations. The uncertainty of the determined uplift rates is about 2 mm yr^{-1} for the TUD sites while that for the GNET sites is well below this value. Bevis et al. (2012) gave the GNET uplift rates an uncertainty measure of less than

Table 1
GNSS-Observed Uplift Rates and Predicted Elastic Displacement Rates at the Sites (TUD: BILD to ROME, GNET: BLAS to YMER)

Station	Latitude (°N)	Longitude (°W)	nC	tS (yr)	tE (yr)	GNSS rates (mm yr^{-1})	Elastic rates (mm yr^{-1})
BILD	78.11644	23.50335	2	2008.6	2016.6	4.9 ± 2.4	4.5 ± 1.2
BLAF	79.53292	22.64949	3	2008.6	2017.5	7.2 ± 1.6	4.5 ± 1.0
CENT	80.19141	21.72366	3	2008.6	2017.5	5.8 ± 1.9	3.2 ± 0.5
CRIW	80.09245	24.31355	4	2008.6	2017.5	4.9 ± 1.8	4.0 ± 1.6
FRAN	78.57844	18.62732	4	2008.6	2017.7	4.6 ± 2.0	3.2 ± 0.4
HOLM	80.27302	16.43152	3	2008.6	2016.6	5.6 ± 1.7	4.6 ± 2.8
HOVG	79.70018	18.23056	2	2008.6	2016.6	6.4 ± 1.8	3.8 ± 2.0
LAMW	79.22646	22.30611	3	2008.6	2017.5	8.9 ± 1.7	7.0 ± 2.6
MUSK	79.97955	22.72291	2	2009.6	2017.7	5.4 ± 1.9	3.4 ± 0.4
ROME	81.07179	22.97472	2	2008.6	2017.5	5.1 ± 1.7	3.6 ± 2.0
BLAS	79.53861	22.97472	5	2008.6	2017.7	7.1 ± 1.6	4.7 ± 1.3
GMMA	77.80943	19.65212	4	2009.6	2017.7	5.0 ± 1.8	2.8 ± 0.2
GROK	78.44270	22.90376	5	2008.6	2017.7	6.9 ± 1.6	5.2 ± 0.9
LEFN	80.45668	26.29346	5	2008.6	2017.7	5.6 ± 1.6	3.6 ± 1.0
NORD	81.60014	16.65545	–	–	–	–	2.8 ± 0.8
NRSK	79.15503	17.72542	5	2008.6	2017.7	5.4 ± 1.6	3.1 ± 0.4
YMER	7743289	24.32633	4	2009.6	2017.7	2.8 ± 1.6	2.4 ± 1.2

Note. In addition to the site's position, the number of GNSS measurement campaigns nC, start time tS and end time tE of the overall observation period are stated. The elastic rates were predicted from our preferred mass-change estimate version C3 (as discussed in the main text) by using the Caron GIA model and the data combination over the period July 2010 to June 2017.
Abbreviations: GIA, glacial-isostatic adjustment; GNSS, Global Navigation Satellite System

1 mm yr^{-1} (spanning a time period of less than 3 years) while Khan et al. (2016) derived 0.2 mm yr^{-1} (time span 6–7 years, and 8.5 years for Station NORD). The inferred uncertainty for the campaign style measurements well reflects the difference to the GNET permanent recordings considering the different set-up of the measurements and the much fewer number of observations. Nevertheless, it is a realistic measure, and the inferred uplift rates are statistically significant. The colocation of the TUD installation BLAF and the GNET site BLAS (Blåsø, north-west shore of NG) allows a direct cross-checking. The DGNSS analysis of campaign style observations yields 7.2 ± 1.6 mm yr^{-1} for BLAF and 7.1 ± 1.6 mm yr^{-1} for BLAS, while Khan et al. (2016) obtained 7.6 ± 0.2 mm yr^{-1} for BLAS in the complete time series analysis (Tables 1 and S1). Also the difference in the observation time span has to be noted (almost 9 vs. 7 years).

3.2. Ice-Mass Change From GRACE

The mission time of GRACE and CryoSat-2 overlap with the interval of the GNSS measurement campaigns in the period July 2010 to June 2017. This period comprises 66 available monthly GRACE solutions. We used the ITSG-Grace2018 series of GRACE solutions up to a maximum spherical harmonic (SH) degree of $n_{max} = 90$ (Kvas et al., 2019; Mayer-Gürr et al., 2018). We substituted the coefficient C_{20} by the more accurate results from satellite laser ranging (SLR) observations (Loomis et al., 2019). Likewise, following Loomis et al. (2019) we replaced the C_{30} coefficients by SLR results in the solutions for November 2016 and later when the shut-down of the accelerometer aboard GRACE-B entailed a high noise level of the GRACE C_{30} series.

GRACE gravity field solutions refer to a reference frame with an origin defined by CM so that degree-one components are zero by definition. Degree-one components caused by mass redistributions at the Earth surface were estimated with respect to the center-of-figure frame following the approaches from Swenson

et al. (2008) and Bergmann-Wolf et al. (2014) and implementing the optimal parameter setup as described by Sun et al. (2016). For this we used the ITSG-Grace2018 coefficients of degree $n \geq 2$ together with estimates of degree-one components of a GRACE-derived change in ocean mass which was uniformly distributed over the ocean. Prior to the inversion for degree one the contribution of GIA has to be removed. We subtracted the gravity field coefficients of each of the three global GIA models (see Section 2) from the GRACE coefficients to calculate three different degree-one time series where each is consistent with one of the different GIA models under investigation. The obtained degree-one components show a spread in their contribution to the estimated Greenland ice-mass trends from −7.04 to −10.49 Gt yr^{-1} (Table S2). The models Huy3 and GNET-GIA were not considered here because they are not globally defined.

Variations in the Earth's gravity field are caused by variations in mass distribution. Gravity field anomalies (and likewise mass anomalies) are referred to as the difference between the gravity field at time t and a mean gravity field. To derive mass anomalies $\Delta m(t)$ at time t over a certain region we started from a regional integration approach (Swenson & Wahr, 2002). In the spatial domain, it reads

$$\Delta m(t) = \iint_{\Omega} \eta(\Omega) \Delta\kappa(\Omega, t) r^2 d\Omega. \tag{5}$$

In the SH domain, it reads

$$\Delta m(t) = 4\pi r^2 \sum_{n=1}^{n_{\max}} \sum_{m=-n}^{n} \eta_{nm} \Delta\kappa_{nm}(t). \tag{6}$$

In Equation 5 the surface integral is defined over a spherical Earth with radius r, where Ω stands for the spatial position on the Earth's surface. $\Delta\kappa(\Omega, t)$ is the surface-mass anomaly in units of mass per surface area (kg m^{-2}) derived from gravity field anomalies (Wahr et al., 1998). $\eta(\Omega)$ is the weighting function employed when integrating the GRACE-based surface-mass anomalies. Owing to the SH representation of GRACE solutions, the mass-change estimation was in fact realized in the SH domain according to Equation 6, where $\kappa_{nm}(t)$ and η_{nm} are the SH coefficients of $\kappa(\Omega, t)$ and $\eta(\Omega)$, respectively. For the coefficients of SH degree n and order $|m|$, $m \geq 0$ and $m < 0$ indicates the cosine and sine dependence, respectively, of the underlying SH base functions on longitude. $\Delta\kappa_{nm}(t)$ were derived from anomalies of the gravity field coefficients (Stokes coefficients) according to Wahr et al. (1998), where we used the elastic load Love numbers for the compressible PREM inferred by H. Wang et al. (2012). Prior to the conversion, the GRACE-observed gravity field coefficients at each epoch have been corrected for GIA using the predicted present-day rate of the GIA-induced change in each coefficient according to the model under investigation.

The weighting functions, or tailored sensitivity kernels η_{nm} (Groh & Horwath, 2016) were developed at TUD within the European Space Agency's climate change initiative (ESA CCI) project (ESA, 2018). They were determined in a formal least squares optimization that minimized the sum of the variances of propagated GRACE errors and leakage effects. The leakage variance was modeled based on assumptions of signal variances at positions within the ice sheet area and in far-field regions, respectively, and their propagation to leakage errors. GRACE errors were characterized by an empirical error covariance matrix. The sensitivity kernels were designed for 728 integration regions individually, each shaped as a square of 50 × 50 km^2, which form the cells of a polar-stereographic grid (EPSG:3413) covering Greenland's ice-covered areas. The time series of gridded (gravimetric) mass anomalies $\Delta\dot{\kappa}_j^{\mathrm{G}}$ (for $j = 1, ..., 728$) are given in units of mass per grid cell area: $\Delta\dot{\kappa}_j^{\mathrm{G}} = \Delta m_j \,/\, a_j$. The results per grid cell were summed up to larger aggregations such as drainage basins or the entire ice sheet depending on the application. Linear trends $\Delta\dot{\kappa}_j^{\mathrm{G}}$ were estimated by simultaneously fitting linear, periodic (1 year, half a year, 161 days) and quadratic terms to the time series of gridded surface-mass anomalies with a reference time at the midpoint of the entire observational period (Figure 3a). Terms with the period of 161 days account for an alias period arising from errors in the S2 tide correction (Ray & Luthcke, 2006).

The GIA effect was removed according to either of the models A13, ICE-6G and Caron, termed as versions G1, G2, and G3, respectively. We denote the effect of the GIA correction on the estimated ice-mass change as "GIA mass effect" (positive if the GIA correction makes the estimated trend smaller, i.e., less positive or more negative). Note that the GIA mass effect depends on the employed estimation method (our sensitivity kernels η_{nm}), besides depending on the specific GIA model. For Greenland's ice-covered regions the GIA mass

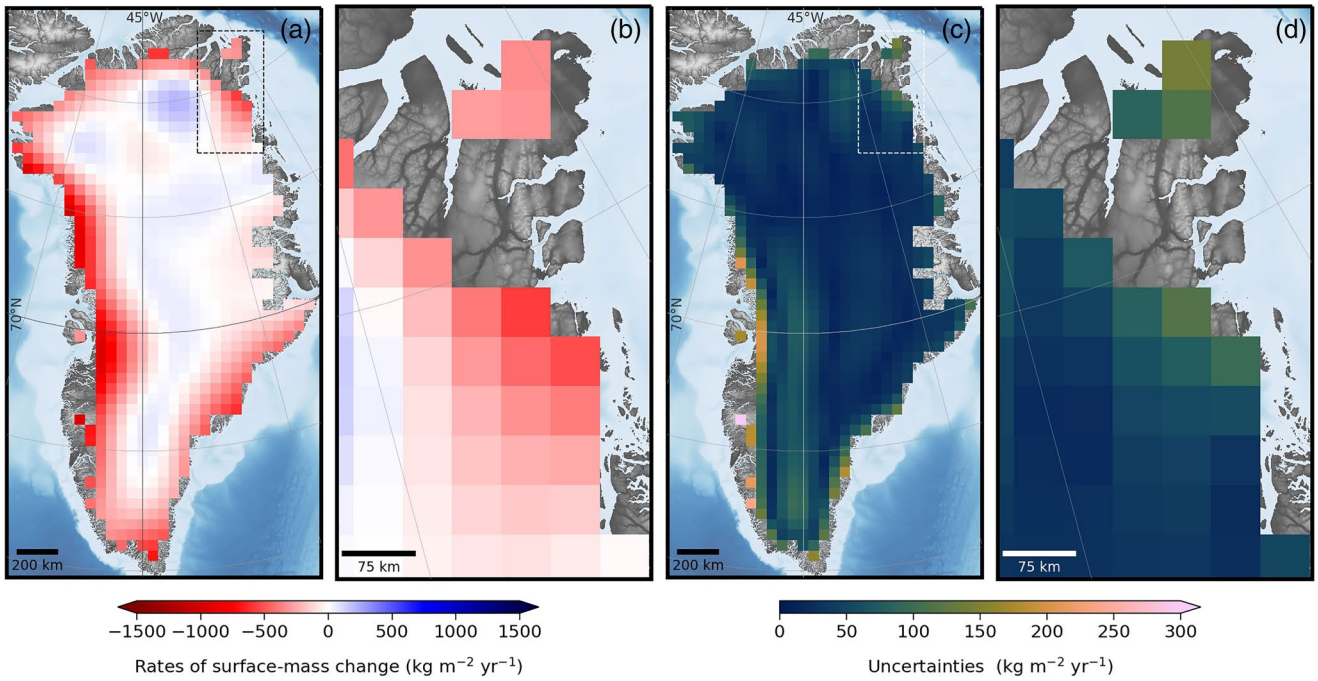

Figure 3. (a and b) Mass-change rates and (c and d) their uncertainties derived from GRACE version G3 (based on the Caron GIA model) over the period from July 2010 to June 2017. (b and d) Show an enlarged view of our study area. GIA, glacial-isostatic adjustment; GRACE, Gravity Recovery and Climate Experiment.

effect of Caron is 10.8 Gt yr^{-1} while the mass effects of A13 and ICE-6G are roughly zero (Table 2). Adopting the Caron model, the GIA mass effect accounts for 4.3% of the Greenland ice-mass estimate, which is in the range indicated by Wake et al. (2016). To quantify the GIA mass effect in north-east Greenland we de-

Table 2

GIA-Induced Volume-Change Rates $\Delta\dot{V}^{\mathrm{GIA}}$*, Rates of Altimetry-Derived Ice-Volume Change* $\Delta\dot{V}^{\mathrm{A}}$*, GIA Mass Effect* $\Delta\dot{M}^{\mathrm{GIA}}$ *and Rates of Gravimetry-Derived Ice-Mass Change* $\Delta\dot{M}^{\mathrm{G}}$ *According to the GIA Models A13, ICE-6G and Caron for the Period July 2010 to June 2017*

GIA model	$\Delta\dot{V}^{\mathrm{GIA}}$ (km^3 yr^{-1})	$\Delta\dot{V}^{\mathrm{A}}$ (km^3 yr^{-1})	$\Delta\dot{M}^{\mathrm{GIA}}$ (Gt yr^{-1})	$\Delta\dot{M}^{\mathrm{G}}$ (Gt yr^{-1})
Greenland				
1 A13	−0.99	−199.81	0.02	−235.38
2 ICE-6G	0.08	−200.90	0.79	−237.66
3 Caron	1.32	−202.17	10.83	−249.64
Basin NE1				
1 A13	0.18	−3.65	1.15	−6.29
2 ICE-6G	0.32	−3.79	1.18	−6.54
3 Caron	0.17	−3.63	1.19	−6.80
Basin NE2				
1 A13	0.40	−3.92	3.07	−7.79
2 ICE-6G	0.58	−4.10	3.28	−8.25
3 Caron	0.33	−3.84	2.34	−7.61

Note. The results are listed for Greenland and two drainage basins NE1 and NE2 (Figure 4).
Abbreviation: GIA, glacial-isostatic adjustment.

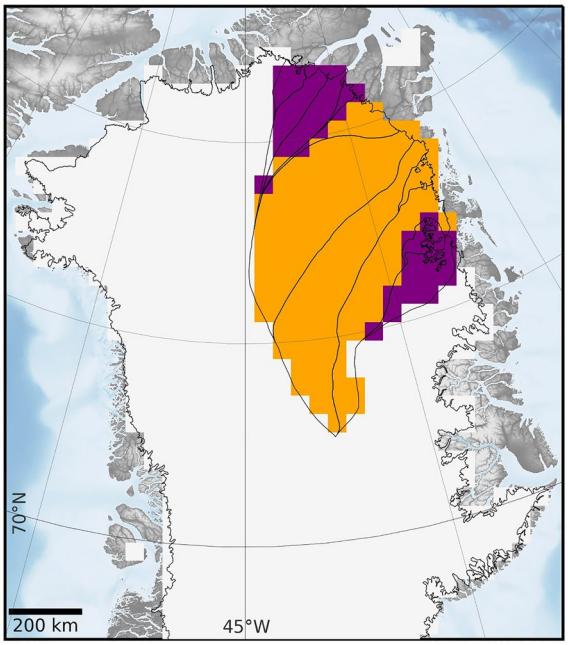

Figure 4. Investigated drainage basins in north-east Greenland. Basin NE1 (orange) combines the branches of NG, ZI, Kofoed-Hansen Bræ, and SN. Basin NE2 (NE1 plus purple extension) incorporates the areas up to Hagen Bræ in the north and L. Bistrup Bræ in the south. Basin definitions are given according to Mouginot et al. (2019).

fine drainage basin NE1 that combines the major branches of NEGIS. For this basin the GIA mass effect is 17.6%, 18.3%, and 18.1% of the ice-loss rate if Caron, A13 and ICE-6G were applied, respectively (Table 2). The percentage of the GIA mass effect would be even larger for an alternative basin definition NE2 which additionally includes glacier catchment areas north and south of NE1 (Figure 4). For basin NE2 the GIA mass effects are 30.8%, 39.4%, and 39.8% of the ice-mass change.

To assess the uncertainty of $\Delta\dot{\kappa}^{\mathrm{G}}$ (Figure 3c) we considered the formal uncertainty of the trend, uncertainties of the externally added time series of C_{20} and degree-one terms, and effects of signal leakage:

$$\sigma_{\Delta\dot{\kappa}^{\mathrm{G}}}{}^2 = \sigma_{\mathrm{formal}}{}^2 + \sigma_{C_{20}}{}^2 + \sigma_{\mathrm{deg1}}{}^2 + \sigma_{\mathrm{leak}}{}^2. \tag{7}$$

One-sigma uncertainties associated with C_{20} and degree-one terms were derived by the spread of an ensemble of available solutions, involving five C_{20} time series (Cheng & Ries, 2017; Cheng et al., 2013; König et al., 2019; Loomis et al., 2019; Sun et al., 2016) and six to ten degree-one time series (Tables S3 and S2). The assessment of uncertainties associated to leakage errors depends on our established combination strategy and is, therefore, explained later in Section 4.2.1. We did not include GIA uncertainties. Rather, we apply the alternative GIA models in a deterministic sense in order to eventually assess their consistency with geodetic observations.

3.3. Surface-Elevation Change From CryoSat-2

Surface-elevation changes were estimated using CryoSat-2 Baseline C Level 2I data. We analyzed altimeter records from July 2010 to June 2017, the overlap period with the GRACE time series (see Section 3.2). Over the GrIS, CryoSat-2 operates in two distinct modes (Wingham et al., 2006). While the rather flat interior is covered by the low resolution mode (LRM), the interferometric synthetic aperture radar (SARIn) mode is applied at the steep margins to enhance along-track resolution and to obtain the point of closest approach in across-track direction. LRM data were slope-corrected and retracked as described by Krieger, Strößenreuther et al. (2020) using a 10% threshold retracker. SARIn data were processed and provided by Helm et al. (2014).

The further processing utilizes the method of repeat altimetry analysis (RAA; e.g., Legrésy et al., 2006; McMillan et al., 2014; Sandberg Sørensen et al., 2018; Schröder et al., 2019). It was implemented on a polar-stereographic grid with 1.5×1.5 km^2 spacing (EPSG:3413) for the entire GrIS and for the main part of Flade Isblink to derive a mean rate of surface-elevation changes from the altimeter height measurements. For each RAA grid cell we used all satellite-observed heights h_{sat} at time t_i and position (x_i, y_i) (relocated for LRM) within a search radius of 2.5 km of the cell's center coordinate (x_0, y_0). To separate the desired elevation changes from topographic features the local topography in a cell was considered prior to the estimation of elevation changes by

$$\begin{aligned} h(x_0, y_0, t_i) &= h_{\mathrm{sat}}(x_i, y_i, t_i) \\ &\quad -(h_{\mathrm{topo}}(x_i, y_i) - h_{\mathrm{topo}}(x_0, y_0)). \end{aligned} \tag{8}$$

The heights h_{topo} were evaluated from the ArcticDEM with a spatial resolution of 100 m (Porter et al., 2018). A least squares model was fitted to the topography-corrected heights h:

$$\begin{aligned} h(x_0, y_0, t_i) &= h_0 + \Delta\dot{h}^{\mathrm{A}}(t_i - t_0) \\ &\quad + b_1 \sin(2\pi t_i) + b_2 \cos(2\pi t_i) \\ &\quad + s_i + \epsilon_i. \end{aligned} \tag{9}$$

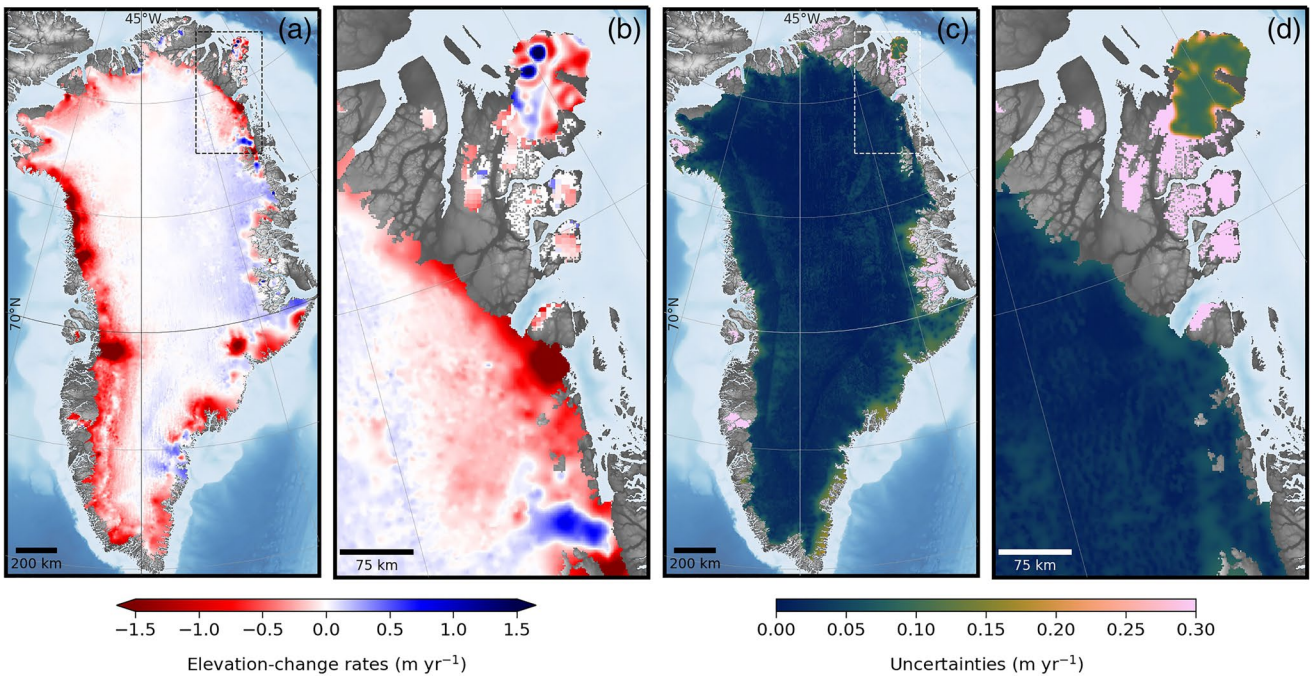

Figure 5. (a and b) Elevation-change rates and (c and d) their uncertainties derived from CryoSat-2 repeat altimetry analysis over the period from July 2010 to June 2017. (b and d) Show an enlarged view of our study area.

h_0 describes the absolute elevation at (x_0, y_0). $\Delta\dot{h}^{A}$ is the desired rate of (altimetric) elevation change and t_0 the reference time. Seasonal variations are modeled by sine and cosine terms with the amplitudes b_1 and b_2. The correction s_i accounts for the time-variable penetration of radar signals into the firn (Simonsen & Sørensen, 2017). While penetration effects were already reduced by the choice of the retracker, the term s_i models remaining penetration effects through a regression of h_i against waveform parameters as described by Krieger, Strößenreuther et al. (2020). The difference between the fitted model and the observations is given by the residuals ϵ_i.

Results were rejected as outliers for cells if (a)$|\Delta\dot{h}^{A}| > 20$ m yr^{-1}, (b) a posteriori uncertainty of $\Delta\dot{h}^{A}$ exceeds 1 m yr^{-1}, (c) observations span less than 1 year, (d) a seasonal amplitude exceeds five times an amplitude calculated by the firn densification model IMAU-FDM (Kuipers Munneke et al., 2015; Ligtenberg et al., 2018). Cells were also rejected (e) at the LRM/SARIn mode boundary if they included results from both modes, subject to their inherently different local sampling and to boundary effects of SARIn beam forming (Krieger, Strößenreuther et al., 2020).

Heterogeneous measurement-error filtered kriging (HFK; Christensen, 2011) was implemented to interpolate and filter the successfully solved RAA grid cells. Interpolation and filtering is usually used since the spatial coverage of the RAA estimates is neither homogeneous nor complete (Strößenreuther et al., 2020). By choosing the method of HFK, the filter mechanism is applied based on the RAA a posteriori uncertainties. LRM and SARIn results were jointly processed using HFK. The corresponding spheric variogram model is characterized by a nugget of 0.002 m^2 yr^{-2}, a sill of 0.026 m^2 yr^{-2} and a range of 10 km. The resulting elevation-change rates $\Delta\dot{h}^{A}$ are shown in Figure 5a. The final HFK uncertainty $\sigma_{\Delta\dot{h}^{A}}$ (Figure 5c) was derived by error propagation and was proven to provide a reliable uncertainty estimate (Strößenreuther et al., 2020).

We performed the altimetry analysis for the entire GrIS and for the main part of Flade Isblink, as already mentioned, delineated according to the IMBIE ice mask (Rignot & Mouginot, 2012; Rignot et al., 2011). For

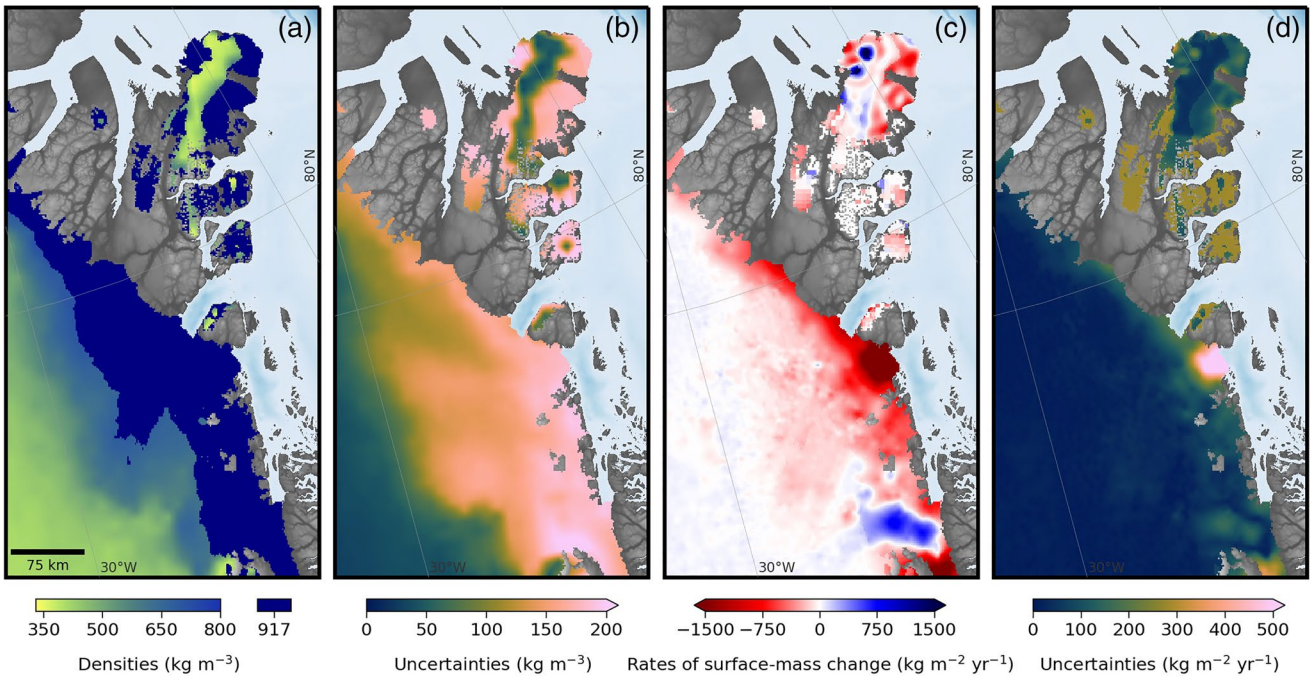

Figure 6. Mass conversion of elevation-change rates: (a) density model and (b) its uncertainties, (c) the resulting mass-change rates from CryoSat-2 with (d) uncertainties. For the whole of Greenland, the density model and the mass-change rates are shown by Figure S2.

the peripheral glaciers except Flade Isblink we adopted mean rates of the surface-elevation change products from the ESA GrIS CCI project (ESA, 2018). The products were provided as 5-year running means by DTU Space covering the period 2011–2017 (Simonsen & Sørensen, 2017).

The CryoSat-2 SARIn mode highly improved the recording of rapid surface-elevation changes at steep slopes in comparison to conventional radar altimeters. Nevertheless, strong thinning rates at the margin of the GrIS cannot be fully captured due to the lower resolution in across-track direction of about 1.5 km (Krieger, Strößenreuther et al., 2020; Simonsen & Sørensen, 2017). By comparing TanDEM-X and CryoSat-2 elevation-change rates at the glacier termini of NG and ZI Krieger, Strößenreuther et al. (2020) reported an evident underestimation of CryoSat-2-inferred surface lowering. This limitation in observing small-scale variations also affects the peripheral glaciers. This is reflected by the maximum HFK uncertainty estimate of 0.3 m yr^{-1} at the edge of Flade Isblink (Figure 5c). We adopted this maximum value as our uncertainty measure for the rates from the ESA CCI product at the peripheral glaciers.

To account for the deformation of the solid Earth the altimetric elevation-change rates $\Delta\dot{h}^{\mathrm{A}}$ were corrected for vertical displacement rates $\Delta\dot{h}^{\mathrm{GIA}}$ predicted by GIA models. The impact of the elastic response was approximated by a scaling factor of $\alpha = 1.0205$ following Groh et al. (2012):

$$\Delta\dot{h}^{\mathrm{cor}} = \alpha \cdot (\Delta\dot{h}^{\mathrm{A}} - \Delta\dot{h}^{\mathrm{GIA}}). \tag{10}$$

We applied each of the three global GIA models (A13, ICE-6G, and Caron) to comply with the GRACE data analysis (see Section 3.2) denoted as versions A1, A2, and A3, respectively. The GIA correction contributes less than 0.7% to Greenland's volume-change rate (Table 2). For the drainage basins NE1 and NE2 the GIA volume signal comprises between 4.6% and 14.2% of the ice-volume signal, which underlines the lower sensitivity of altimetry to GIA than to GRACE.

4. Methods

4.1. Conversion of Surface-Elevation Change to Ice-Mass Change

The corrected elevation-change rates $\Delta\dot{h}^{\mathrm{cor}}$ were converted to rates of surface-mass change $\Delta\dot{\kappa}^{\mathrm{A}}$ (Figure 6c) using

$$\Delta\dot{\kappa}^{\mathrm{A}} = \Delta\dot{h}^{\mathrm{cor}} \cdot \rho \tag{11}$$

where the density ρ is defined as

$$\rho = \begin{cases} \rho^{\mathrm{ice}} & \text{, if } \overline{\dot{\kappa}^{\mathrm{firn}}} < 0 \text{ kg m}^2 \text{ or} \\ & \text{if } |\Delta\dot{h}^{\mathrm{cor}}| > 1 \text{ m yr}^{-1} \text{ and } v^{\mathrm{ice}} > 200 \text{ m yr}^{-1} \\ \rho^{\mathrm{firn}} & \text{, elsewhere.} \end{cases} \tag{12}$$

This density model (Figure 6a) was generated on the basis of SMB predicted by the regional climate model RACMO2.3p2 (Noël et al., 2016, 2018), the firn densification model IMAU-FDM driven by RACMO2.3p2 (Kuipers Munneke et al., 2015; Ligtenberg et al., 2018) and additionally using ice velocity data (Nagler et al., 2015). Mean SMB $\overline{\dot{\kappa}^{\mathrm{firn}}}$ derived from RACMO2.3p2 for the period July 2010 to June 2017 were used to define the equilibrium-line altitude which separates ablation ($\overline{\dot{\kappa}^{\mathrm{firn}}} < 0$) from accumulation area ($\overline{\dot{\kappa}^{\mathrm{firn}}} \geq 0$). In the ablation zone we assumed ice dynamics and surface melt being the main driver of mass variations, which is a widely applied approach (e.g., Sørensen et al., 2011). To include ice-dynamic changes above the equilibrium-line altitude we followed McMillan et al. (2016) and took regions of dynamic imbalance into account. For this purpose, horizontal ice velocity fields v^{ice} from the ESA GrIS CCI project (ESA, 2018) were incorporated. When flow magnitudes exceeding 200 m yr^{-1} in combination with magnitudes of elevation-change rates higher than 1 m yr^{-1} were identified we also applied a density of ice ($\rho^{\mathrm{ice}} = 917$ kg m^{-3}) for the conversion. Elsewhere, firn densities were derived from the IMAU-FDM. Thus, in this region we assumed that surface-elevation changes were dominated by SMB processes. As the original densities were vertically resolved and given with a temporal resolution of 10 days a firn density field was simulated by taking the mean upper density layers (till 1 m) and by averaging over time.

An alternative approach for the conversion from elevation change to surface-mass change is to explicitly account for modeled changes in the firn-column thickness (Hurkmans et al., 2014; Kuipers Munneke et al., 2015). However, this approach, when applied using RACMO2.3p2 and the RACMO-driven firn model, leads to unrealistic positive dynamical imbalance almost all over the GrIS (see Appendix A and a similar experience reported by McMillan et al. [2016]).

The uncertainty of $\Delta\dot{\kappa}^{\mathrm{A}}$ (Figure 6d) is calculated by uncertainty propagation

$$\sigma_{\Delta\dot{\kappa}^{\mathrm{A}}}{}^2 = (\rho \cdot \alpha \cdot \sigma_{\Delta\dot{h}^{\mathrm{A}}})^2 + (\alpha \cdot (\Delta\dot{h}^{\mathrm{A}} - \Delta\dot{h}^{\mathrm{GIA}}) \cdot \sigma_{\rho})^2. \tag{13}$$

The uncertainties of CryoSat-2 elevation-change rates $\sigma_{\Delta\dot{h}^{\mathrm{A}}}$ originated from the altimetry analysis (see Section 3.3). The uncertainty of the density model σ_{ρ} was assessed as the standard deviation of the temporal variations of IMAU-FDM (Figure 6b). The uncertainty of the elastic response factor α was assumed to be negligible. GIA uncertainties were not included in the assessment as the GIA models are applied in a deterministic sense (see Section 3.2).

4.2. Combination of GRACE and CryoSat-2 Results for Refined Ice-Mass Change Estimates

4.2.1. Combination Approach

We considered the ice-mass change estimates from GRACE (Section 3.2) and CryoSat-2 (Section 4.1) as two complementary sets of observations with associated uncertainties. We estimated a new grid of mass-change rates from these two data sets by least squares adjustment. For this purpose we parameterized rates

of ice-mass change $\Delta\dot{m}_k^{\mathrm{C}}$ for the cells $k = 1, ..., n^{\mathrm{C}}$ of a grid. The grid spacing is 1.5×1.5 km^2 in our northeast Greenland study area and coarser at 31.5×31.5 km^2 in the rest of Greenland's ice-covered regions. By maintaining the original spacing of the altimetry grid in the study area we benefit from its ability to resolve changes at glacier scale. The coarser resolution outside the study area, chosen for computational reasons, is sufficient for our purpose of predicting elastic load deformations in the study area. We conducted the combination approach for each of the three global GIA models by considering version G1 and A1 (based on A13), G2 and A2 (based on ICE-6G), G3 and A3 (based on Caron). The resulting estimates from the combination are denoted as C1, C2, C3.

The observation equations for the altimetry-based observations read

$$\Delta\dot{\kappa}_k^{\mathrm{A}} = \frac{1}{a_k} \cdot \Delta\dot{m}_k^{\mathrm{C}} + \epsilon_k^{\mathrm{A}} \tag{14}$$

where a_k is the area of the kth grid cell and $\Delta\dot{\kappa}_k^{\mathrm{A}}$ is the altimetry-based observation of ice-mass change per surface area. ϵ_k^{A} is the residual. For the 1.5×1.5 km^2 cells, $\Delta\dot{\kappa}_k^{\mathrm{A}}$ was directly taken from the altimetry analysis according to Equation 11. For the 31.5×31.5 km^2 cells, $\Delta\dot{\kappa}_k^{\mathrm{A}}$ was derived from averaging the altimetry-based results within the coarser grid cell (Figure S3b).

To establish the observation equations for the GRACE-based observations we refer to Equation 5. Even though each GRACE-based ice-mass change observation $\Delta\dot{\kappa}_j^{\mathrm{G}}$ is associated to a specific, discrete 50×50 km^2 grid cell j ($j = 1, ..., n^{\mathrm{G}}$ with $n^{\mathrm{G}} = 728$), it realizes a spatially extended integral of surface-mass changes employing its specific weight function $\eta_j(\Omega)$. We formulated the observation equation as a discretization of Equation 5 limited to the parametrization domain:

$$\Delta\dot{\kappa}_j^{\mathrm{G}} = \frac{1}{a_j} \cdot \sum_{k=1}^{n^{\mathrm{C}}} \left(\eta_j(\Omega_k) \cdot \Delta\dot{m}_k^{\mathrm{C}} \right) + \epsilon_j^{\mathrm{G}} \tag{15}$$

where Ω_k denotes the spherical position of the kth cell of the parametrization grid and ϵ_j^{G} is the residual of the observation $\Delta\dot{\kappa}_j^{\mathrm{G}}$. We solved Equations 14 and 15 for the set of $\Delta\dot{m}_k^{\mathrm{C}}$ that minimizes the weighted sum of squares of ϵ_k^{A} and ϵ_j^{G}. The definition of weights is explained next.

The stochastic model of the residuals ϵ_k^{A} was summarized in Equation 13. It includes no covariances. The absence of error correlations between cells is a reasonable assumption for the 31.5×31.5 km^2 grid but not for the 1.5×1.5 km^2 grid. To compensate for the neglect of error correlations between 1.5 km grid cells we scaled their uncertainties by the factor $21 = \sqrt{441}$, where 441 is the number of 1.5×1.5 km^2 cells fitting into a 31.5×31.5 km^2 cell. The uncertainty of a mean value over 441 cells is $\sqrt{441}$-times larger in a case of fully correlated errors than in a case of uncorrelated errors (e.g., Koch, 1999). Hence, the scaling factor compensates for the neglect of correlations.

The stochastic model of the residuals ϵ_j^{G} was summarized in Equation 7. However, we still need to specify the assessment of the leakage uncertainty σ_{leak} therein. In the given context leakage arises because Equation 15 models $\Delta\dot{\kappa}_j^{\mathrm{G}}$ as a (discretized) integral restricted to the parametrization domain while in fact $\Delta\dot{\kappa}_j^{\mathrm{G}}$ is a global integral according to Equation 5. Therefore, the residual ϵ_j^{G} contains the contributions from any region outside the parametrization grid to this global integral. We assessed this contribution by means of two synthetic data sets following Groh et al. (2019). We used the linear trend of the monthly ITSG-Grace2018 solutions and excluded mass changes from Greenland. After global mass conservation was ensured by solving for the sea-level equation, the coefficients were applied to the regional integration approach (Equation 6) to infer the first and major part of the leakage uncertainty. Furthermore, ocean-mass variations induced by Greenland's ice-mass changes contribute to the global integral in Equation 5 and need to be considered in the stochastic model of the residuals ϵ_j^{G}. To assess this contribution we described the altimetric ice-mass trend in Stokes coefficients up to degree $n_{\max} = 90$ and solved for the sea-level equation. The resulting RSL change was applied to the regional integration approach to infer the second and minor part

of the leakage uncertainty. All components of the full uncertainty assessment $\sigma_{\Delta\dot{\kappa}^G}$ are shown in Figure S1. Leakage uncertainty derived from the global, linear GRACE trend (masking out Greenland) has the greatest impact on $\sigma_{\Delta\dot{\kappa}^G}$.

The relation between the variances ${\sigma_{\Delta\dot{\kappa}^A}}^2$ and ${\sigma_{\Delta\dot{\kappa}^G}}^2$ was adapted by iteratively estimating two variance components for the two observation types during the least squares adjustment. Figures S3c and S3d show ${\sigma_{\Delta\dot{\kappa}^A}}^2$ and ${\sigma_{\Delta\dot{\kappa}^G}}^2$ scaled with the respective, estimated variance component.

4.2.2. Uncertainty Estimates

We chose two different methods to evaluate uncertainties of the ice-mass change estimates derived from the combination. On the one hand, uncertainties based on the specific a priori information were propagated to estimate an uncertainty for the refined mass-change rates of every grid cell *k*. On the other hand, statistical methods were used to estimate an appropriate uncertainty for regionally integrated mass-change rates.

The a priori, one-sigma uncertainties (Equation 7 and 13) used in the stochastic model of the combination approach considered the following error sources: limitations due to specific characteristics of the respective satellite technique and corrections therein, temporal variations in the firn model and formal errors of the algorithms applied. The a posteriori uncertainties of $\Delta\dot{m}_k^C$ are used to predict the uncertainties of the elastic load deformation at the location of the GNSS sites (see Section 4.3).

Uncertainties of regionally integrated mass-change rates were inferred from the spread of estimates from alternative methods. The alternative methods comprise the refined mass-change estimates from the combination (C1, C2, C3), and mass trends derived from altimetry only (A1, A2, A3) and gravimetry only (G1, G2, G3). For any of these methods the resulting mass-change rate $\Delta\dot{M}_{\text{ref}}$ is given the uncertainty

$$\sigma_{\Delta\dot{M}_{\text{ref}}} = \sqrt{\frac{1}{N}\sum_{i=1}^{N}(\Delta\dot{M}_{\text{ref}} - \Delta\dot{M}_i)^2} \tag{16}$$

where $\Delta\dot{M}_i$ are the estimates based on all considered methods. Their number, *N*, is nine for Greenland, the GrIS and the three drainage basins. *N* is six for the peripheral glaciers where methods G1, G2, and G3 do not apply.

4.3. Prediction of Elastic Load Deformation

For the prediction of the elastic load deformation in north-east Greenland we used estimates of (a) Greenland's ice-load changes, (b) load variations of the surrounding ocean, (c) mass redistributions on a global scale. The deformation effect from (c) was evaluated in the SH domain by using load Love numbers (e.g., van Dam et al., 2007) based on GRACE SH solutions with degree-one components and atmospheric and oceanic background fields added and GIA subtracted. It reflects the deformation due to the long-wavelength part of the load, which is sufficient for the far field of load changes. In the near field, we assessed the high-resolution load from (a) the refined Greenland mass-change estimates from our combination and (b) fingerprints of RSL change calculated by Adhikari et al. (2019) within a distance of 300 km to Greenland's coast. We subtracted the GRACE-based load changes from the high-resolution load to get the short-wavelength part of the load, which is not resolved by GRACE. The Green's function approach (Farrell, 1972) was then used to predict the additional elastic deformation due to this short wavelength part of the near field. We applied the Green's function for vertical displacements, as tabulated by H. Wang et al. (2012) for a compressible PREM. The used Green's functions and load Love numbers refer to the reference frame CM, since CryoSat-2 data, GNSS measurements and GIA models are defined in CM.

The inclusion of the short-wavelength load in the near field is important, as it increases the predicted elastic rates in north-east Greenland by up to a factor six. The inclusion of load changes other than Greenland ice masses is also important. If we accounted exclusively for the Greenland ice-mass changes by convolving them with the Green's function, the predicted elastic rates in the study area would be smaller by 0.4 mm yr^{-1} (A13), 0.5 mm yr^{-1} (ICE-6G), and 0.7 mm yr^{-1} (Caron) than if we additionally accounted for (b) and (c).

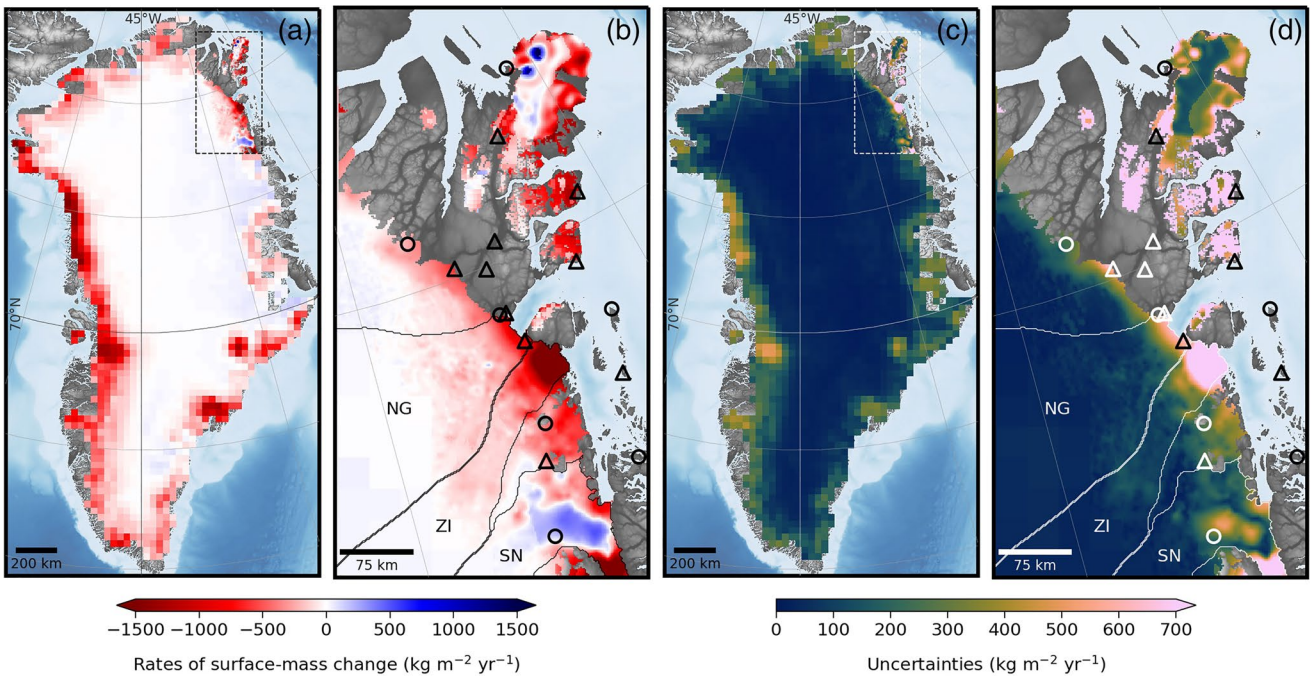

Figure 7. Results from the combination analysis version C3: (a and b) mass-change rates and (c and d) their uncertainties. (b and d) Show an enlarged view of our study area including the drainage basins of NG, ZI, SN as well as the locations of TUD GNSS sites (triangle) and GNET sites (circle). GNET, Greenland GPS network; GNSS, Global Navigation Satellite System; TUD, Technische Universität Dresden.

The results depend on the GIA model since the GRACE solutions used to evaluate (c) were GIA corrected. The contribution of the nearby ocean to the elastic deformation is maximum 0.04 mm yr^{-1} and we neglect its dependence on GIA. The a posteriori, one-sigma uncertainties of the Greenland ice-mass change were propagated to the Green's function approach to assess the uncertainties of the elastic prediction. An uncertainty of the Green's function due to uncertainties of the Earth rheology was not included. Uncertainties of the deformation effects of the nearby ocean and the far field were neglected since their contribution to the elastic prediction is far below the uncertainty assessment of the GNSS uplift rates (Table 1).

5. Results and Discussion

5.1. Refined Ice-Mass Change Estimates

Figure 7 shows the combined rates of surface-mass change over Greenland and their a posteriori uncertainties for version C3 (based on the Caron GIA model). Unless stated otherwise, figures and presented results refer to this version. In our study area largest mass loss was estimated at the terminus of ZI. For the entire drainage basin of ZI we determined a mass-change rate of -3.7 ± 1.3 Gt yr^{-1} (Table S4). The neighboring catchment area, the drainage basin of NG, reveals much lower rates of change (-0.9 ± 0.4 Gt yr^{-1}). For the basin of SN the estimated ice-mass rate is close to zero (-0.5 ± 0.5 Gt yr^{-1}). The refined estimates exhibit massive thinning at the lower part and broad thickening at the upper part of the glacier area since SN is in a quiescent phase after a surge (see Section 2). Our results for ZI and SN agree with Mouginot et al. (2019) within the reported uncertainties. For the drainage basin of NG, our result, though complying with Krieger, Strößenreuther et al. (2020) (-1.0 ± 1.0 Gt yr^{-1}), disagree with the result from the mass-budget method by Mouginot et al. (2019) (-3.5 ± 0.2 Gt yr^{-1}). The tendency that results from the mass-budget method are more negative than results from altimetry and GRACE is known and unresolved for Greenland in general (Shepherd et al., 2019), and likewise the discrepancy beyond stated uncertainties found here for the NG basins remains unresolved. For the comparisons to the two studies the respective drainage basin delineations according to Mouginot et al. (2019) and Krieger, Floricioiu et al. (2020) were used (Figure S4). For the peripheral glaciers in north-east Greenland we largely estimated negative rates of mass change. However,

Table 3
Comparison of the Rates of Altimetry-Derived Ice-Mass Change $\Delta\dot{M}^{\mathbf{A}}$, the Rates of Gravimetry-Derived Ice-Mass Change $\Delta\dot{M}^{\mathbf{G}}$ and the Results From the Combined Mass-Change Analysis $\Delta\dot{M}^{\mathbf{C}}$

GIA model	$\Delta\dot{M}^{\mathbf{A}}$(Gt yr^{-1})	$\Delta\dot{M}^{\mathbf{G}}$(Gt yr^{-1})	$\Delta\dot{M}^{\mathbf{C}}$(Gt yr^{-1})
1 A13	−158.4 ± 63.3	−235.4 ± 44.5	−227.9 ± 40.7
2 ICE-6G	−159.0 ± 62.8	−237.7 ± 45.8	−230.1 ± 41.7
3 Caron	−159.4 ± 62.4	−249.6 ± 53.9	**−232.8 ± 43.1**

Note. Estimates are given for a parametrization of the GrIS and all peripheral glaciers as shown in Figure 7. The three different versions refer to the three GIA models considered: A13 (1), ICE-6G (2), and Caron (3). Our preferred estimate, indicated in bold, is the one using the Caron GIA model and the data combination version C3 (as discussed in the text).
Abbreviation: GIA, glacial-isostatic adjustment.

distinct thickening rates were detected for two northern surging glaciers of FI, similar to the spatial patterns illustrated in Rinne et al. (2011) and Gardner et al. (2013).

The Greenland ice-mass trend over the period July 2010 to June 2017 is estimated to −233 ± 43 Gt yr^{-1} (Table 3, version C3). These refined ice-mass change estimates are in good agreement with rates published by Bamber et al. (2018) (−247 ± 15 Gt yr^{-1} for the period 2012–2016) and Shepherd et al. (2019) (−244 ± 28 Gt yr^{-1} for the period 2012–2017). The GrIS contributes 87% (−202 ± 35 Gt yr^{-1}) to Greenland's total ice-mass loss while the peripheral glaciers account for 13% (−31 ± 19 Gt yr^{-1}) (Table S5). The mass trend of Greenland's peripheral glaciers from our combination approach is in the range of estimates by previous studies (Bamber et al., 2018; Hock et al., 2019; Meredith et al., 2019; Zemp et al., 2019, see also Table S6). Therefore, it is important to specify whether peripheral glaciers were included in the mass-balance analysis of Greenland or not.

Mass-change estimates from GRACE are very sensitive to the choice of the applied GIA model in contrast to estimates from CryoSat-2. Thus, the three combination products (C1, C2, C3) differ because of the different GRACE-based inputs (G1, G2, G3) whose gridded mass-change estimates were assigned to the refined parametrization grid during the adjustment (see Section 4.2.1) depending mainly on the altimetric uncertainties and the sensitivity kernels according to Equation 15. Thus, the spatial pattern of the differences between the three combination results is dominated by the spatial distribution of the uncertainties of the altimetric mass-change rates (Figure S6). Furthermore, it reflects the spatial pattern of the differences in the GIA correction. Mass-loss estimates from version C3 are smaller than from version C1 and C2 (Figures S6d and S6e) because the GIA mass effect of the Caron model is smaller than the GIA mass effect of the models A13 and ICE-6G in the study region (Figures S6a and S6b). This can also be seen when comparing the mass-loss rates for basin NE2 (Table S5) and the corresponding GIA mass effects (Table 2). For entire Greenland, in contrast, version C3 suggests the strongest mass-loss estimate among the three combination results (Table 3) because the GIA mass effect of the Caron model is higher than the GIA mass effect of the models A13 and ICE-6G (Table 2).

Section 5.4.1 further discusses the influence of the mass-change estimates from GRACE and CryoSat-2 on the combination and compares results from only GRACE, only CryoSat-2 and the data combination.

5.2. Predicted Elastic Load Deformation

Figure 8a displays vertical elastic displacement rates of the study area predicted from combination version C3. A maximum uplift of 13.8 mm yr^{-1} was predicted near the front of ZI where mass loss is largest. The GNSS station closest to these vast ice-mass changes is LAMW located at the western edge of Lambert Land where NG and ZI separate. LAMW has the strongest elastic response prediction among all stations (7.0 ± 2.6 mm yr^{-1}) mainly influenced by ZI's state of mass imbalance. The minimum elastic displacement among all GNSS sites (2.4 ± 1.2 mm yr^{-1}) was predicted for YMER next to the upper part of SN which exhibits mass gain. For the sites apart from LAMW and YMER we predicted an elastic response in the range of 2.8–5.2 mm yr^{-1} (Table 1).

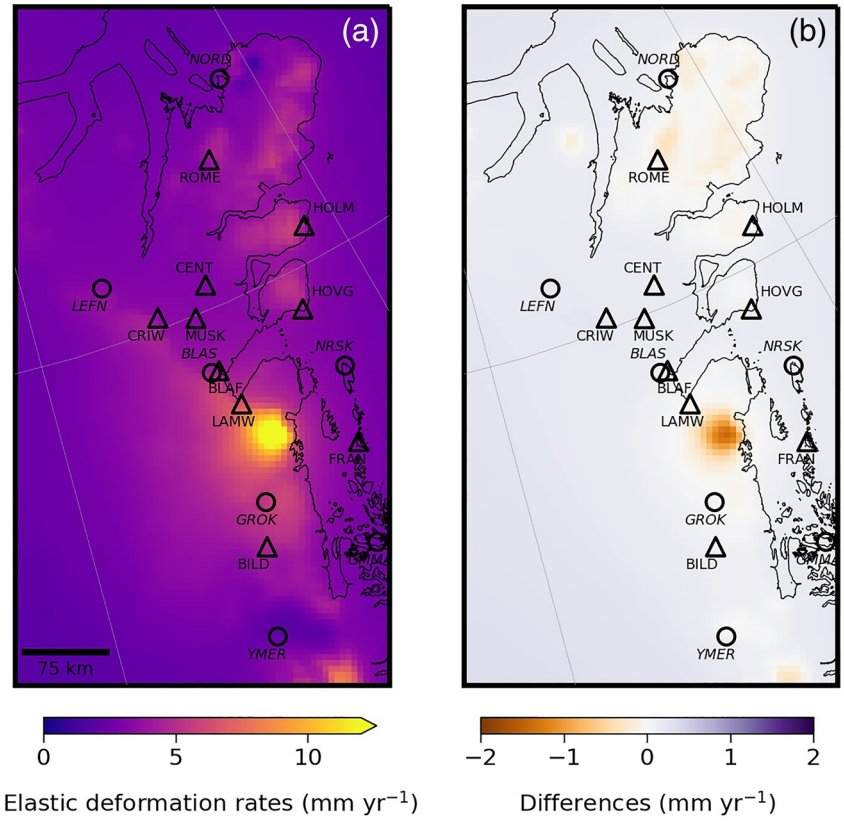

Figure 8. (a) Vertical elastic displacement rates of the study area predicted from the combined mass-change estimates version C3. (b) Differences in the elastic prediction depending on the adopted GIA model: version C3–C1. Locations of TUD GNSS sites (triangle) and GNET sites (circle) are shown in addition. GIA, glacial-isostatic adjustment; GNET, Greenland GPS network; GNSS, Global Navigation Satellite System; TUD, Technische Universität Dresden.

The elastic predictions by Khan et al. (2016) agree with ours within the uncertainties for four out of seven GNET station positions (Table S1). Apart from the site LEFN, the elastic rates predicted by this study are higher than those from Khan et al. (2016). At the site NORD, located at the north-western edge of Flade Isblink, the predictions differ most (by 1.5 mm yr^{-1}). Discrepancies can be explained by the different time intervals and by the different methods including the used data sets and their spatial extent to derive ice-load estimates. While we combined data from GRACE and CryoSat-2 considering peripheral glaciers, Khan et al. (2016) used measurements from CryoSat-2 and NASA's Airborne Topographic Mapper without the inclusion of peripheral glaciers. Furthermore, we note that the uncertainty estimates by this study are more conservative (Table 1) compared to the estimates given by Khan et al. (2016) (Table S1) since we accounted for correlations between the altimetric observations in north-east Greenland (Section 4.2).

Figure 8b illustrates differences between the elastic displacement rates inferred from the combined analysis C3 and C1. Large differences occur at ZI with a value of −1.4 mm yr^{-1}. The spatial pattern of the differences in the elastic deformation is related to the pattern of the differences between the mass-change estimates C3 and C1 and, thus, to the uncertainties of the altimetric mass-change rates (see Section 5.1 and Figure S6d). However, for the GNSS stations the impact of the assumed GIA model on elastic uplift rates is in a small range of 0–0.2 mm yr^{-1} (Table S7). These discrepancies are not significant for they are smaller than the uncertainties of the elastic predictions.

5.3. Validation of Bedrock-Displacement Predictions Implied by Alternative GIA Models

To obtain the total vertical displacement we added the rate of the GIA model under investigation to the elastic rate. The GIA displacement rates and the total displacement rates at the GNSS sites, predicted by using

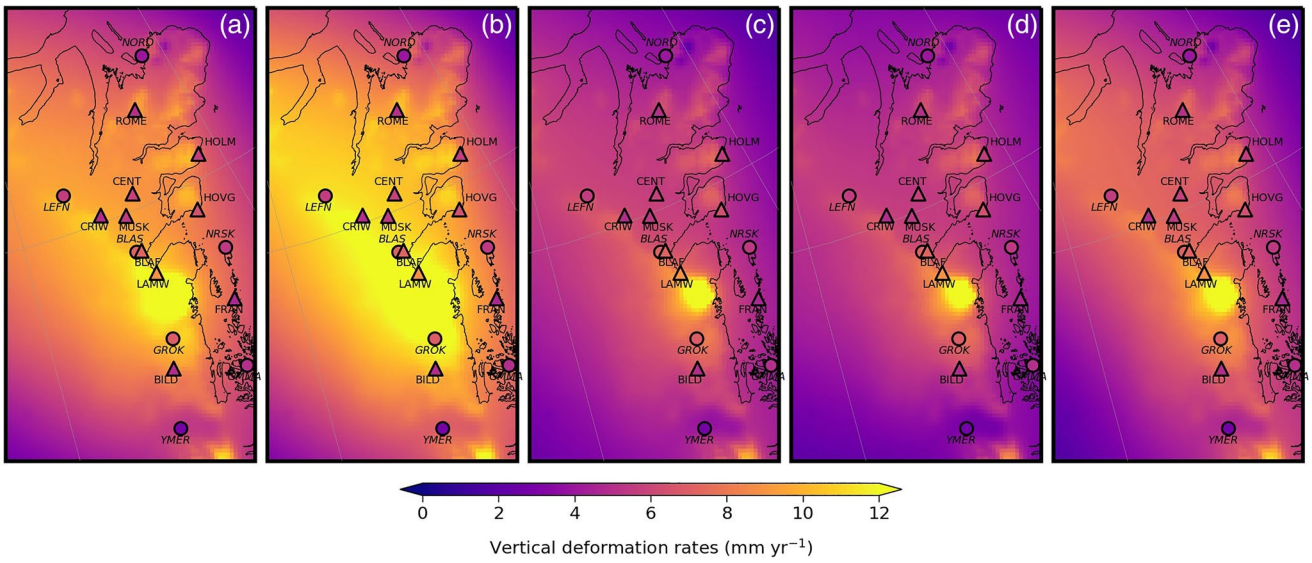

Figure 9. Predicted vertical displacement rates from the sum of the elastic response derived from the combined mass-change estimates and the respective GIA model: (a) version C1 based on A13, (b) version C2 based on ICE-6G, (c) version C3 based on Caron, (d) version C4 based on Huy3, (e) version C5 based on GNET-GIA. Predictions are displayed against results from GNSS at TUD sites (filled triangles) and GNET sites (filled circles). The color scale is identical to that of Figures 2 and 8a. GIA, glacial-isostatic adjustment; GNET, Greenland GPS network; GNSS, Global Navigation Satellite System; TUD, Technische Universität Dresden.

the different GIA models, are given in Tables S8 and S9, respectively. The models Huy3 and GNET-GIA were not included in the combination strategy (see Section 3.2) but were considered for the total predicted rates (denoted as versions C4 and C5, respectively). In these cases we chose the elastic estimates of version C3, noting the low sensitivity of the elastic prediction to the choice among the global GIA models under consideration (see Section 5.2).

Predicted rates from versions C1 to C5 are plotted against GNSS observations in Figure 9. Predictions using A13 (C1, Figure 9a) and ICE-6G (C2, Figure 9b) are larger than the GNSS observations, unlike Caron (C3, Figure 9c), Huy3 (C4, Figure 9d), and GNET-GIA (C5, Figure 9e) which are more similar to the GNSS results. For versions C3, C4, and C5 the uncertainty range of the predicted uplift rates at each GNSS site overlap with the uncertainty ranges of the GNSS results (Figure 10). Hence, the GIA models Caron, Huy3, and GNET-GIA are compatible with the observations from GRACE, CryoSat-2, and GNSS in north-east Greenland. In contrast, predictions C1 and C2 are systematically higher than the GNSS rates, so that the related uncertainty ranges do not overlap at 10 (C1) and 15 (C2) out of 17 stations.

For GNET-GIA (Khan et al., 2016) an agreement to GNSS rates is expected since their model was adjusted to fit their GNSS observations. Huy3 (Lecavalier et al., 2014), also a regional model, did not incorporate any GNSS data but comprehensive records of past ice extent and RSL. However, this model also agrees well with the GNSS rates. In contrast, Caron et al. (2018) included only few RSL observations and did not integrate any GNSS records in Greenland (see Section 2). Nevertheless, the GNSS results confirm their modeled GIA rates in north-east Greenland. A13 (A et al., 2013) and ICE-6G (Peltier et al., 2015, 2018) overestimate GIA in the region of study. The two models used the same reconstruction of the Greenland glacial history, however, the overestimation by ICE-6G is even stronger than that by A13. We note that even though we validate the signal from three GIA model outputs, there is still uncertainty (nonuniqueness) in terms of the two primary model inputs, the ice-load history and the Earth model.

Figure 10 further illustrates how the uncertainties of the predicted rates vary with position, which is related to the uncertainties of the ice-mass change estimates (Figure 7d). For the positions further away from the mass changes (GMMA, FRAN, MUSK, NRSK, CENT) the uncertainty is ≤0.5 mm yr^{-1}. Near ZI and for positions close to peripheral glaciers (LAMW, HOVG, ROME, HOLM) the uncertainty is ≥2.0 mm yr^{-1}. The

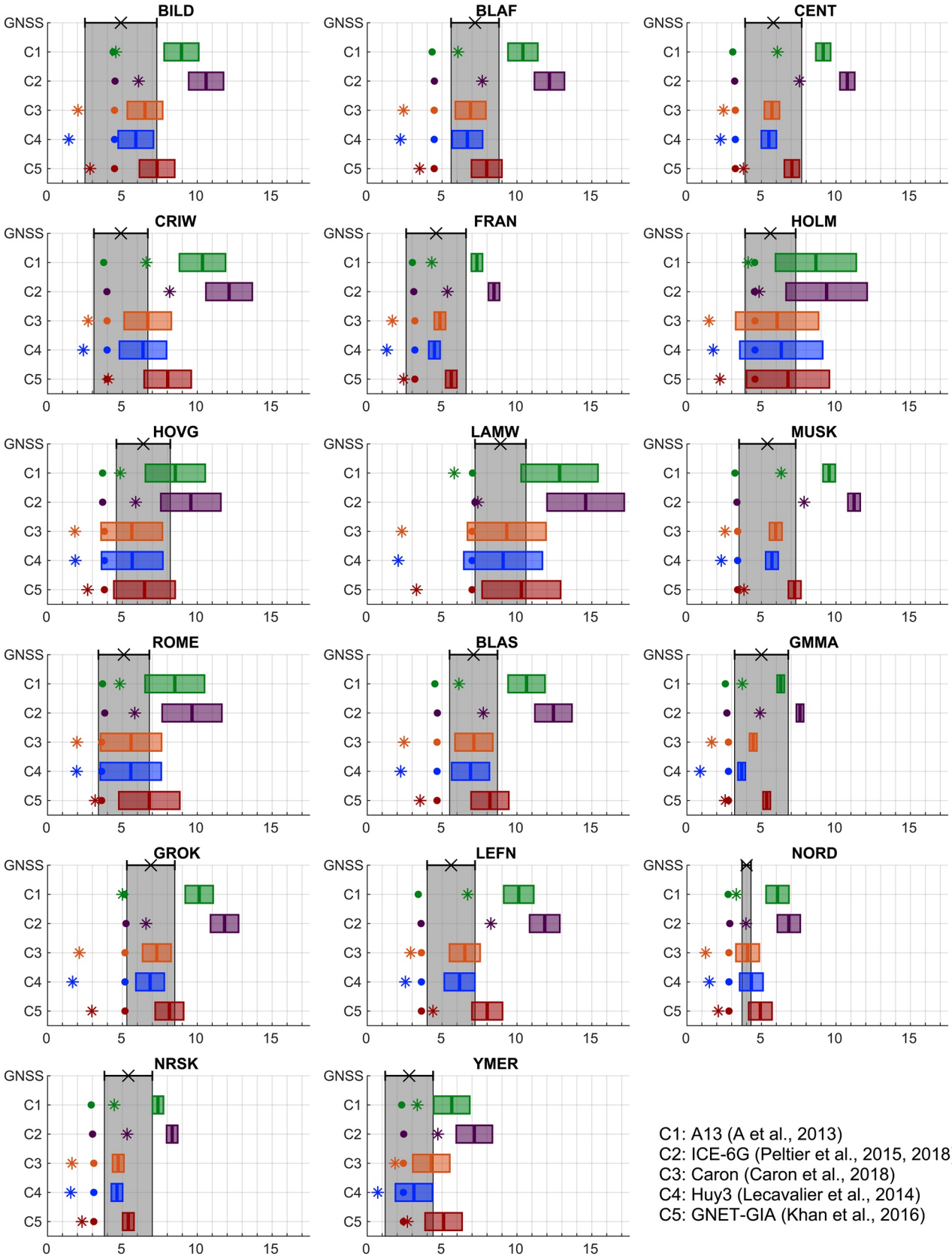

C1: A13 (A et al., 2013)
C2: ICE-6G (Peltier et al., 2015, 2018)
C3: Caron (Caron et al., 2018)
C4: Huy3 (Lecavalier et al., 2014)
C5: GNET-GIA (Khan et al., 2016)

uncertainty measures of the GNSS-observed rates are related to the number of measurement campaigns (Table 1). Station NORD is given a low uncertainty (0.2 mm yr^{-1}) as here we rely on the results from Khan et al. (2016) (see Section 3.1 and Table S1).

5.4. Sensitivity to Methodological Choices for the Ice-Mass Change Estimates

Here we assess the advantages of the altimetry-gravimetry combination strategy with account for peripheral glaciers, as compared to alternative approaches of ice-mass change estimates. We note, however, that comparisons with GNSS rates do not have the discriminative power to validate the related improvements of elastic predictions. This is due to their additional sensitivity to the GIA prediction, the involved uncertainties, and the fact that the GNSS sites are not exactly situated where concentrated load changes occur.

5.4.1. Comparisons to Results Using Only GRACE or Only CryoSat-2

Altimetry alone estimated significantly less negative mass trends (-159 ± 62 Gt yr^{-1} for entire Greenland, -155 ± 55 Gt yr^{-1} for the GrIS, -4 ± 19 Gt yr^{-1} for the peripheral glaciers) than the data combination (Table S5). Shepherd et al. (2019) noted that altimetry results tend to be less negative than results from satellite gravimetry and the mass-budget method. They also report a range of 121 Gt yr^{-1} (for 2005–2015) between different altimetry-based estimates. The difference between our preferred combined estimate and the altimetry-only estimate for entire Greenland (Table 3, last line) is 73 Gt yr^{-1}. Reasons why radar altimetry may underestimate mass losses include the systematic undersampling of the low-lying surfaces of outlet glaciers because the altimeter measurement (in SARIn modus) refers to the closest surface point within its (Doppler beam-formed) footprint (Krieger, Strößenreuther et al., 2020; Thomas et al., 2008). The part of the glaciers thus undersampled are particularly subject to dynamically induced losses as well as to surface melting.

The combination constrains the overall mass-balance estimate toward the GRACE-only estimate (-250 ± 54 Gt yr^{-1}) which is a significant improvement over the altimetry-only estimate. The combination further maintains the spatial pattern of the altimetry input which is a significant improvement over the gravimetry-only estimate especially in terms of the spatial resolution and allocation of mass changes to single glaciers. In the adjustment altimetry-based observations of grid cells with a low uncertainty were given a high weight. Therefore, the combined mass estimates of those grid cells are only slightly influenced by the gravimetry-based observations. In contrast, for the grid cells with high altimetric uncertainties the combination results are largely constrained by the Greenland-wide GRACE-derived mass changes and differ largely from the altimetry-based estimates (Figure S7a). As we obtain a larger mass loss signal from GRACE than from altimetry, compared to the altimetry-derived estimates the combination reduces mass gain at the upper part of SN and intensifies mass loss at the termini of ZI and SN as well as at the peripheral glaciers (Figure S7b). For this reason, the mass-loss rate over the basin ZI is larger from the combination than from altimetry or gravimetry alone. Similarly, over the basin SN the combination results exhibit slight negative rates while altimetry and gravimetry show slight positive rates (Table S4).

Using altimetric mass estimates smaller displacement rates were predicted in north-east Greenland than using the combination approach (Figure S7c). The differences have a maximum of 3.5 mm yr^{-1} at Holm Land. The differences between elastic predictions inferred from the combination and from gravimetric mass estimates reach maximum values of 8.0 and 5.9 mm yr^{-1} at the termini of ZI and SN where concentrated ice-load changes occur (Figure S7d). For the estimates at the GNSS sites, HOLM experiences the strongest influence of the combined mass analysis. There, the elastic predictions from altimetry and gravimetry are smaller than the refined estimate from the combination with values of 2.5 and 2.0 mm yr^{-1}, respectively

Figure 10. Validation of the predicted vertical displacement rates against GNSS displacement rates at the TUD and GNET stations. The *x*-axis shows the displacement rates in mm yr^{-1}. Gray boxes represent the GNSS measurements and their one-sigma uncertainty ranges. Colored boxes show the total predicted rates from version C1 to C5 and their one-sigma uncertainty ranges. Points and asterisks additionally show the split between the two components, the elastic displacement and the GIA uplift rates, respectively. GIA, glacial-isostatic adjustment; GNET, Greenland GPS network; GNSS, Global Navigation Satellite System; TUD, Technische Universität Dresden.

(Tables 1 and S10). Considering the GIA Caron model, at HOLM the total predictions from altimetry and gravimetry are smaller than the measured GNSS uplift rates with values of 2.0 and 1.6 mm yr^{-1}, respectively (Figures S9, S10h, and S10m).

5.4.2. Sensitivity to the Inclusion of Peripheral Glacier Estimates

Previous studies have typically analyzed the mass balance of the ice sheets and of glaciers and ice caps separately as well as by applying different methods (Bamber et al., 2018; Hanna et al., 2020; Marzeion et al., 2017; Noël et al., 2017). An overview of past studies on Greenland's peripheral glaciers and their considered outlines (e.g., according to the RGI Consortium, 2017) is given in Table S6. To examine the significance of mass changes from peripheral glaciers we compared the results from version C3 to predictions based on a combined (GRACE-CryoSat-2) analysis excluding peripheral glaciers (denoted as C3_ex). Hence, in the observation Equations 14 and 15 the parameters $\Delta\dot{m}_k^C$ for pixels k belonging to peripheral glaciers were deleted, leading to the deletion of the corresponding Equation 14 and modification of each of the Equation 15.

The approach excluding peripheral glaciers estimated an ice-mass trend of -212 ± 37 Gt yr^{-1} for the GrIS, 10 Gt yr^{-1} more negative than the approach including peripheral glaciers regarding the ice sheet area. Mass loss was also suggested to be greater for the drainage basins of ZI and NG compared to the results from version C3 (Table S11). Differences in rates of surface-mass change and in the elastic prediction between C3 and C3_ex occur mainly at the ice sheet margin and at peripheral glaciers (Figure S8). In north-east Greenland at the ice sheet margin the elastic predictions from version C3 are smaller than from C3_ex (by up to 2.2 mm yr^{-1}) because in C3 part of GRACE's mass contribution was allocated to the peripheral glaciers (Table S12). Accordingly, at the peripheral glaciers the elastic predictions from C3 are larger than the elastic predictions from C3_ex (by up to 3.8 mm yr^{-1} at Holm Land). Regarding the GNSS sites the inclusion of peripheral glaciers in the combined mass analysis has the greatest impact on HOLM (difference of 2.5 mm yr^{-1}). At HOLM the total prediction from C3_ex is 2.0 mm yr^{-1} smaller than the GNSS observations (Figures S9 and S10r).

6. Conclusion

In this study, we presented first results from TUD GNSS campaign measurements in north-east Greenland which took place between 2008 and 2017. In addition to the TUD sites, we processed records from the GNET stations in this region and thus, could extend the analysis from Khan et al. (2016) by 2 years. The results from our study and from Khan et al. (2016) confirm each other. Vertical rates of bedrock displacement are in the range from 2.8 mm yr^{-1} (at YMER near the upper part of SN where ice is thickening) to 8.9 mm yr^{-1} (at LAMW between the outlets of NG and ZI where ice is massively thinning).

We used the independent GNSS measurements to validate predicted vertical displacement rates inferred from the sum of refined elastic estimates and GIA-induced displacements. Thereby, we investigated five different GIA models. Among all GNSS sites a minimum (2.4 mm yr^{-1}) and maximum (7.0 mm yr^{-1}) elastic deformation rate was predicted at YMER and LAMW, respectively. For the whole region the elastic prediction revealed its maximum at the terminus of ZI (13.8 mm yr^{-1}). The total bedrock-displacement predictions implied by the model of Caron et al. (2018), the models Huy3 (Lecavalier et al., 2014), and GNET-GIA (Khan et al., 2016) were validated by the GNSS uplift rates within the uncertainty ranges of the predicted and measured rates. These three GIA models suggest a relatively small GIA signal at the GNSS sites: 1.3–2.9 mm yr^{-1} (Caron), 0.7–2.5 mm yr^{-1} (Huy3), and 2.1–4.4 mm yr^{-1} (GNET-GIA). In contrast, GIA rates at the GNSS sites modeled by ICE-6G (Peltier et al., 2015, 2018) and by the model A13 (A et al., 2013) are in the range of 4.0–8.3 and 3.3–6.7 mm yr^{-1}, respectively. We demonstrate that the two models ICE-6G and A13 overestimate GIA in north-east Greenland since the total predictions yielded by these GIA models are systematically higher than the GNSS rates.

We combined GRACE and CryoSat-2 data to refine ongoing ice-mass change estimates and infer improved predictions of the elastic response. The combination approach resolved ice-mass changes in north-east

Greenland at glacier scale (grid resolution of 1.5 × 1.5 km^2) and included peripheral glaciers. Over the period July 2010 to June 2017 Greenland's ice-mass trend is −233 ± 43 Gt yr^{-1}, whereby the GrIS and peripheral glaciers contribute 87% and 13%, respectively. We demonstrated the impact of ice-mass changes from peripheral glaciers not only on Greenland's mass balance estimate but also on the predictions of bedrock displacement in the study area. Neglecting peripheral glaciers would lead to an underestimation of the predicted rates at locations near peripheral glaciers.

The complementarity of satellite altimetry and satellite gravimetry benefits the refined ice-mass change estimates from the combination: while the spatial resolution of the altimetric elevation changes is maintained, Greenland's mass balance estimate is adjusted to GRACE. The integration of gravimetric mass-balance estimates constrains the altimetric difficulties of converting volume to mass and of capturing elevation changes in steep terrain. However, these difficulties are still reflected in the high uncertainties of the combined estimates especially seen at the border of the ice sheet and at peripheral glaciers. For future work, mass-balance estimates of individual outlet glaciers can be improved by including records from imaging satellite missions, high-resolution interferometric SAR techniques, CryoSat-2 swath processing or satellite and airborne laser altimetry to the GRACE-CryoSat-2 combination. In doing so, small-scale variations which are not resolved by conventional CryoSat-2 SARIn processing could be accounted for.

A consistent treatment of the GIA effect based on model predictions was achieved throughout the whole analysis. This applies to the following processing steps: adding external degree-one terms for the monthly GRACE solutions, GIA correction of gravimetric mass-change and altimetric volume-change estimates, and derivation of the total predicted bedrock displacements. The independent GNSS measurements further enabled the evaluation of gravimetric ice-mass change estimates which are in particular affected by uncertainties of the GIA contribution. We showed that the GIA mass effect of north-east Greenland is about 31% of the ice-mass change rate according to the validated Caron GIA model and the regional integration approach employed. Even though our findings narrow down the GIA correction in north-east Greenland as reported by Barletta et al. (2013), the estimated GIA mass effect is still significant. In contrast to the Caron model, ICE-6G or A13 (which overpredict GIA uplift rates in this region) suggested a GIA mass effect of about 40% of the ice-loss. These estimates corroborate the need for more accurate GIA models, particularly when studying individual drainage basins.

Appendix A: Conversion of Elevation Change to Mass Changes—An Alternative Method

An alternative method to convert surface-elevation change to mass change uses modeled variations in firn-column thickness $\Delta\dot{h}^{\text{firn}}$ (Hurkmans et al., 2014; Kuipers Munneke et al., 2015). $\Delta\dot{h}^{\text{firn}}$ were derived from the RACMO-driven firn densification model IMAU-FDM (Kuipers Munneke et al., 2015; Ligtenberg et al., 2018) (Figure A1a) and removed from $\Delta\dot{h}^{\text{cor}}$ to obtain ice-dynamical elevation-change rates $\Delta\dot{h}^{\text{d}} = \Delta\dot{h}^{\text{cor}} - \Delta\dot{h}^{\text{firn}}$ (Figure A1b). In the following, $\Delta\dot{h}^{\text{d}}$ were converted to an ice-dynamical mass signal $\Delta\dot{\kappa}^{\text{d}} = \rho^{\text{ice}} \cdot \Delta\dot{h}^{\text{d}}$. In doing so, changes in the firn column that are only causing variations in volume and not in mass (compaction, percolation and refreezing of melt water) were already considered. Finally, rates of surface-mass change due to SMB processes $\Delta\dot{\kappa}^{\text{firn}}$ (Figure A1c) were added back by the regional climate model RACMO2.3p2 (Noël et al., 2016, 2018) to gain the total altimetric mass-balance estimate $\Delta\dot{\kappa}^{\text{A}} = \Delta\dot{\kappa}^{\text{d}} + \Delta\dot{\kappa}^{\text{firn}}$ (Figure A1d).

The change rates in firn-column thickness and surface mass exhibit different spatial pattern mainly in the interior of the GrIS above the equilibrium-line altitude: $\Delta\dot{\kappa}^{\text{firn}}$ is close to zero while $\Delta\dot{h}^{\text{firn}}$ is lowering over the period July 2010 to June 2017. This is explainable due to variations in firn compaction and an increase in surface melt with melt water refreezing in the firn column (S. Ligtenberg, personal communication, 2018).

However, subtracting $\Delta\dot{h}^{\text{firn}}$ from the altimetry-derived $\Delta\dot{h}^{\text{cor}}$ caused unrealistic ice-dynamical thickening across the interior and several areas at the ice sheet's margin. Most likely, the reason for these discrepan-

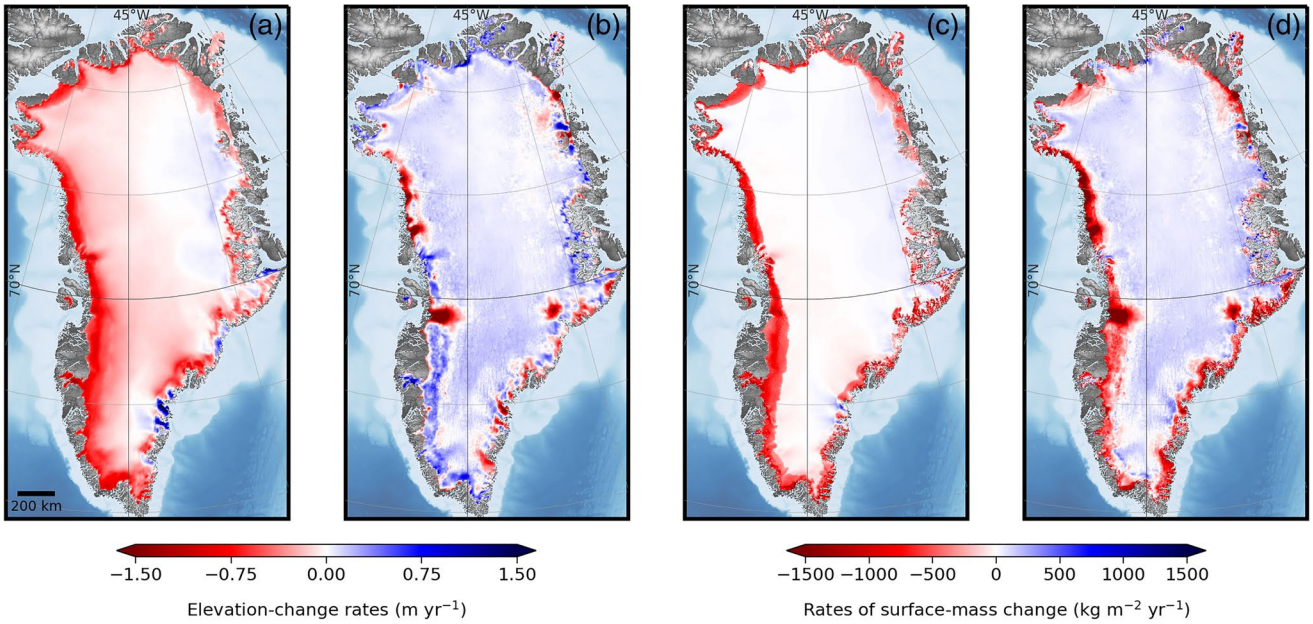

Figure A1. Mass conversion of elevation-change rates - method 2: (a) rates of firn-column thickness changes $\Delta\dot{h}^{\mathrm{firn}}$, (b) resulting ice-dynamical elevation-change rates $\Delta\dot{h}^{\mathrm{d}}$, (c) rates of cumulative SMB changes $\Delta\dot{\kappa}^{\mathrm{firn}}$ (c), (d) resulting total mass-change rates $\Delta\dot{\kappa}^{\mathrm{A}}$

cies is a combined effect of errors in RACMO2.3p2 and the altimetry product. On the one hand, changing penetration into the surface and volume scattering are high uncertainty factors of radar altimeters. Despite these time-variable effects were modeled in our analysis, uncertainties remain. Furthermore, a possible underestimation of surface lowering from CryoSat-2 regarding the margins of the GrIS and the peripheral glaciers was already discussed in Section 3.3.

On the other hand, an overestimation of decreasing firn-column thickness is possible as well: Biases of surface melt in the RACMO2.3p2 time series would have a different effect on $\Delta\dot{h}^{\mathrm{firn}}$ and $\Delta\dot{\kappa}^{\mathrm{firn}}$ as surface melt directly affects the firn densification model in contrast to the SMB in the regional climate model (S. Ligtenberg, personal communication, 2018). Beyond that, $\Delta\dot{\kappa}^{\mathrm{firn}}$ are rates of cumulative SMB anomalies referring to a reference SMB defined over the period 1960–1979 for which the climate is assumed to be in equilibrium (Kuipers Munneke et al., 2015). The choice of the reference period has a big impact on the time series of cumulative SMB anomalies and, thus, on the inferred linear rates (van den Broeke et al., 2009; Wouters et al., 2015). An uncertainty of about 20 Gt yr^{-1} was indicated by van den Broeke et al. (2009) in the linear rate.

Data Availability Statement

Predictions of the GIA model ICE-6G_D (VM5a) are available at https://www.atmosp.physics.utoronto.ca/~peltier/data.php and at supporting information of Peltier et al. (2018). Predictions of the GIA model Caron et al. (2018) can be downloaded from https://vesl.jpl.nasa.gov/solid-earth/gia. The monthly GRACE solutions were obtained from https://www.tugraz.at/institute/ifg/downloads/gravity-field-models/itsg-grace2018/. We thank the European Space Agency for providing the altimetry data products and V. Helm (AWI) for processing and providing CryoSat-2 SARIn data. The refined ice-mass change estimates from this study are available as gridded data set at PANGAEA (https://doi.org/10.1594/PANGAEA.922884). GNSS-derived uplift rates and the elastic prediction at the GNSS sites are provided by this paper.

Acknowledgments
The field work was supported by the Alfred Wegener Institute Helmholtz Centre for Polar and Marine Research (AWI), Bremerhaven (Germany), during numerous scientific expeditions. For their support we would like to thank the master, the chief scientist and the entire ship and scientific crew of the following cruises of R/V "Polarstern": ARK-XXIII/1 (2008, U. Pahl, G. Budéus), ARK-XXIII/2 (2008, U. Pahl, G. Katt-ner), ARK-XXIV/3 (2009, S. Schwarze, W. Jokat), ARK-XXVII/1 (2012, S. Schwarze, A. Beszczynska-Möller), PS100 (2016, S. Schwarze, T. Kanzow), PS109 (2017, T. Wunderlich, T. Kanzow). Also, the authors like to thank the scientists (PI: A. Humbert), engineers and technicians of AWI for their commitment to realize the 2017 iGRIFF land expedition to north-east Greenland. Many thanks to all (former and present) colleagues and students of our institute who participated and helped in the field work. This work was supported by funds of the German Federal Ministry of Education and Research (BMBF) (project Greenland Ice Sheet/Ocean Interaction [GROCE], Grant no. 03F0778G), the German Research Foundation (DFG) (grant no. HO 4232/2-1), and the European Space Agency (Climate Change Initiative project on the Greenland Ice Sheet, grant 4000112228/15/I-NB). S.A. Khan acknowledges support from the INTAROS (grant no. 727890) funded by European Union's Horizon 2020 Research and Innovation program. The provision of the GIA model A13 (J. Wahr and G. A) is greatly acknowledged. The authors thank G. Milne for providing the output of the GIA model Huy3 (Lecavalier et al., 2014). P. Kuipers Munneke and B. Noël are acknowledged for providing the density profiles of IMAU-FDM and the SMB output of RACMO 2.3p2. We would like to thank Surendra Adhikari, Glenn Milne, and Pippa Whitehouse for their constructive and detailed reviews which helped us to improve the manuscript.

References

A, G., Wahr, J., & Zhong, S. (2013). Computations of the viscoelastic response of a 3-D compressible Earth to surface loading: An application to Glacial Isostatic Adjustment in Antarctica and Canada. *Geophysical Journal International*, *192*(2), 557–572. https://doi.org/10.1093/gji/ggs030

Adhikari, S., Ivins, E., Frederikse, T., Landerer, F., & Caron, L. (2019). Sea-level fingerprints emergent from GRACE mission data. *Earth System Science Data*, *11*(2), 629–646. https://doi.org/10.5194/essd-11-629-2019

Altamimi, Z., Rebischung, P., Métivier, L., & Collilieux, X. (2016). ITRF2014: A new release of the International Terrestrial Reference Frame modeling nonlinear station motions. *Journal of Geophysical Research: Solid Earth*, *121*(8), 6109–6131. https://doi.org/10.1002/2016JB013098

Bamber, J., Westaway, R., Marzeion, B., & Wouters, B. (2018). The land ice contribution to sea level during the satellite era. *Environmental Research Letters*, *13*(6), 063008. https://doi.org/10.1088/1748-9326/aac2f0

Barletta, V., Sørensen, L., & Forsberg, R. (2013). Scatter of mass changes estimates at basin scale for Greenland and Antarctica. *Cryosphere*, *7*(5), 1411–1432. https://doi.org/10.5194/tc-7-1411-2013

Bergmann-Wolf, I., Zhang, L., & Dobslaw, H. (2014). Global eustatic sea-level variations for the approximation of geocenter motion from grace. *Journal of Geodetic Science*, *4*(1). https://doi.org/10.2478/jogs-2014-0006

Bevis, M., Wahr, J., Khan, S., Madsen, F., Brown, A., Willis, M., et al. (2012). Bedrock displacements in greenland manifest ice mass variations, climate cycles and climate change. *Proceedings of the National Academy of Sciences of the United States of America*, *109*(30), 11944–11948. https://doi.org/10.1073/pnas.1204664109

Blewitt, G., Kreemer, C., Hammond, W., & Gazeaux, J. (2016). MIDAS robust trend estimator for accurate GPS station velocities without step detection: MIDAS trend estimator for GPS velocities. *Journal of Geophysical Research: Solid Earth*, *121*(3), 2054–2068. https://doi.org/10.1002/2015JB012552

Boehm, J., Werl, B., & Schuh, H. (2006). Troposphere mapping functions for GPS and very long baseline interferometry from European Centre for Medium-Range Weather Forecasts operational analysis data. *Journal of Geophysical Research*, *111*, B02406. https://doi.org/10.1029/2005JB003629

Bolch, T., Sandberg Sørensen, L., Simonsen, S., Mölg, N., Machguth, H., Rastner, P., & Paul, F. (2013). Mass loss of Greenland's glaciers and ice caps 2003-2008 revealed from ICESat laser altimetry data. *Geophysical Research Letters*, *40*(5), 875–881. https://doi.org/10.1002/grl.50270

Caron, L., Ivins, E., Larour, E., Adhikari, S., Nilsson, J., & Blewitt, G. (2018). GIA model statistics for GRACE hydrology, cryosphere, and ocean science. *Geophysical Research Letters*, *45*(5), 2203–2212. https://doi.org/10.1002/2017GL076644

Cheng, M., & Ries, J. (2017). The unexpected signal in GRACE estimates of C_{20}. *Journal of Geodynamics*, *91*(8), 897–914. https://doi.org/10.1007/s00190-016-0995-5

Cheng, M., Tapley, B., & Ries, J. (2013). Deceleration in the Earth's oblateness. *Journal of Geophysical Research*, *118*(2), 740–747. https://doi.org/10.1002/jgrb.50058

Choi, Y., Morlighem, M., Rignot, E., Mouginot, J., & Wood, M. (2017). Modeling the response of Nioghalvfjerdsfjorden and Zachariae Isstrøm glaciers, Greenland, to ocean forcing over the next century. *Geophysical Research Letters*, *44*(21), 11071–11079. https://doi.org/10.1002/2017GL075174

Christensen, W. (2011). Filtered kriging for spatial data with heterogeneous measurement error variances. *Biometrics*, *67*(3), 947–957. https://doi.org/10.1111/j.1541-0420.2011.01563.x

Citterio, M., & Ahlstrøm, A. (2013). Brief communication "The aerophotogrammetric map of Greenland ice masses". *The Cryosphere*, *7*(2), 445–449. https://doi.org/10.5194/tc-7-445-2013

Colgan, W., Abdalati, W., Citterio, M., Csatho, B., Fettweis, X., Luthcke, S., et al. (2015). Hybrid glacier Inventory, Gravimetry and Altimetry (HIGA) mass balance product for Greenland and the Canadian Arctic. *Remote Sensing of Environment*, *168*, 24–39. https://doi.org/10.1016/j.rse.2015.06.016

Dach, R. Lutz, S. Walser, P. & Fridez P.(Eds.), (2015). *Bernese GNSS software version 5.2*. Bern: Astronomical Institute, University of Bern, Bern Open Publishing. https://doi.org/10.7892/boris.72297

Dach, R., Schaer, S., Arnold, D., Kalarus, M., Prange, L., Stebler, P., et al. (2020). *CODE final product series for the IGS*. Astronomical Institute, University of Bern. https://doi.org/10.7892/boris.75876.4

Dziewonski, A., & Anderson, D. (1981). Preliminary reference Earth model. *Physics of the Earth and Planetary Interiors*, *25*(4), 297–356. https://doi.org/10.1016/0031-9201(81)90046-7

ESA (2018). *Greenland ice sheet CCI: Products*. Norway: European Space Agency and Science and Technology AS. Retrieved from http://esa-icesheets-greenland-cci.org/products

Evans, J., Ó Cofaigh, C., Dowdeswell, J., & Wadhams, P. (2009). Marine geophysical evidence for former expansion and flow of the Greenland Ice Sheet across the north-east Greenland continental shelf. *Journal of Quaternary Science*, *24*(3), 279–293. https://doi.org/10.1002/jqs.1231

Farrell, W. (1972). Deformation of the Earth by surface loads. *Reviews of Geophysics and Space Physics*, *10*(3), 761–797. https://doi.org/10.1029/RG010i003p00761

Fleming, K., & Lambeck, K. (2004). Constraints on the Greenland Ice Sheet since the Last Glacial Maximum from sea-level observations and glacial-rebound models. *Quaternary Science Reviews*, *23*(9–10), 1053–1077. https://doi.org/10.1016/j.quascirev.2003.11.001

Forsberg, R., Sørensen, L., & Simonsen, S. (2017). Greenland and Antarctica Ice Sheet mass changes and effects on global sea level. *Surveys in Geophysics*, *38*(1), 89–104. https://doi.org/10.1007/s10712-016-9398-7

Fritsche, M., Dietrich, R., Knöfel, C., Rülke, A., Vey, S., Rothacher, M., & Steigenberger, P. (2005). Impact of higher-order ionospheric terms on GPS estimates. *Geophysical Research Letters*, *32*, L23311. https://doi.org/10.1029/2005GL024342

Funder, S., & Hansen, L. (1996). The Greenland ice sheet—A model for its culmination and decay during and after the last glacial maximum. *Bulletin of the Geological Society of Denmark*, *42*, 137–152.

Gardner, A., Moholdt, G., Cogley, J., Wouters, B., Arendt, A., Wahr, J., et al. (2013). A reconciled estimate of glacier contributions to sea level rise: 2003 to 2009. *Science*, *340*(6134), 852–857. https://doi.org/10.1126/science.1234532

Groh, A., Ewert, H., Scheinert, M., Fritsche, M., Rülke, A., Richter, A., et al. (2012). An investigation of glacial isostatic adjustment over the Amundsen Sea sector, West Antarctica. *Global and Planetary Change*, *98–99*, 45–53. https://doi.org/10.1016/j.gloplacha.2012.08.001

Groh, A., & Horwath, M. (2016). The method of tailored sensitivity kernels for GRACE mass change estimates. *Geophysical Research Abstracts*, *18*, EGU2016-12065. Retrieved from http://meetingorganizer.copernicus.org/EGU2016/EGU2016-12065.pdf

Groh, A., Horwath, M., Horvath, A., Meister, R., Sørensen, L., Barletta, V., et al. (2019). Evaluating GRACE mass change time series for the Antarctic and Greenland Ice Sheet—Methods and results. *Geosciences*, *9*(10), 415. https://doi.org/10.3390/geosciences9100415

Gunter, B., Didova, O., Riva, R., Ligtenberg, S., Lenaerts, J., King, M., et al. (2014). Empirical estimation of present-day Antarctic glacial isostatic adjustment and ice mass change. *Cryosphere*, *8*(2), 743–760. https://doi.org/10.5194/tc-8-743-2014

Hanna, E., Pattyn, F., Navarro, F., Favier, V., Goelzer, H., van den Broeke, M., et al. (2020). Mass balance of the ice sheets and glaciers—Progress since AR5 and challenges. *Earth-Science Reviews*, *201*, 102976. https://doi.org/10.1016/j.earscirev.2019.102976

Helm, V., Humbert, A., & Miller, H. (2014). Elevation and elevation change of Greenland and Antarctica derived from CryoSat-2. *Cryosphere*, *8*(4), 1539–1559. https://doi.org/10.5194/tc-8-1539-2014

Hock, R., Rasul, G., Cáceres, B., Gruber, S., Hirabayashi, Y., Jackson, M., Steltze, H. (2019). *IPCC special report on the ocean and cryosphere in a changing climate* (pp. 131–202). Retrieved from https://www.ipcc.ch/srocc/chapter/chapter-2/

Hurkmans, R., Bamber, J., Davis, C., Joughin, I., Khvorostovsky, K., Smith, B., & Schoen, N. (2014). Time-evolving mass loss of the Greenland Ice Sheet from satellite altimetry. *Cryosphere*, *8*(5), 1725–1740. https://doi.org/10.5194/tc-8-1725-2014

Huybrechts, P. (2002). Sea-level changes at the LGM from ice-dynamic reconstructions of the Greenland and Antarctic ice sheets during the glacial cycles. *Quaternary Science Reviews*, *21*, 203–231.

Khan, S., Aschwanden, A., Bjørk, A., Wahr, J., Kjeldsen, K., & Kjær, K. (2015). Greenland ice sheet mass balance: A review. *Reports on Progress in Physics*, *78*(4), 046801. https://doi.org/10.1088/0034-4885/78/4/046801

Khan, S., Kjær, K., Bevis, M., Bamber, J., Wahr, J., Kjeldsen, K., et al. (2014). Sustained mass loss of the northeast Greenland ice sheet triggered by regional warming. *Nature Climate Change*, *4*, 292–299. https://doi.org/10.1038/nclimate2161

Khan, S., Sasgen, I., Bevis, M., van Dam, T., Bamber, J., Wahr, J., et al. (2016). Geodetic measurements reveal similarities between post-Last Glacial Maximum and present-day mass loss from the Greenland ice sheet. *Science Advances*, *2*(9), e1600931. https://doi.org/10.1126/sciadv.1600931

King, M., Altamimi, Z., Boehm, J., Bos, M., Dach, R., Elosegui, P., et al. (2010). Improved constraints on models of glacial isostatic adjustment: A review of the contribution of ground-based geodetic observations. *Surveys in Geophysics*, *31*(5), 465–507. https://doi.org/10.1007/s10712-010-9100-4

Koch, K.-R. (1999). *Parameter estimation and hypothesis testing in linear models* (2nd ed.). Springer Berlin Heidelberg.

König, R., Schreiner, P., & Dahle, C. (2019). *Monthly estimates of C(2,0) generated by GFZ from SLR satellites based on GFZ GRACE/GRACE-FO RL06 background models V. 1.0*. https://doi.org/10.5880/GFZ

Krieger, L., Floricioiu, D., & Neckel, N. (2020). Drainage basin delineation for outlet glaciers of Northeast Greenland based on Sentinel-1 ice velocities and TanDEM-X elevations. *Remote Sensing of Environment*, *237*, 111483. https://doi.org/10.1016/j.rse.2019.111483

Krieger, L., Strößenreuther, U., Helm, V., Floricioiu, D., & Horwath, M. (2020). Synergistic use of single-pass interferometry and radar altimetry to measure mass loss of NEGIS outlet glaciers between 2011 and 2014. *Remote Sensing*, *12*(6), 996. https://doi.org/10.3390/rs12060996

Kuipers Munneke, P., Ligtenberg, S., Noël, B., Howat, I., Box, J., Mosley-Thompson, E., et al. (2015). Elevation change of the Greenland Ice Sheet due to surface mass balance and firn processes, 1960–2014. *Cryosphere*, *9*(6), 2009–2025. https://doi.org/10.5194/tc-9-2009-2015

Kvas, A., Behzadpour, S., Ellmer, M., Klinger, B., Strasser, S., Zehentner, N., & Mayer-Gürr, T. (2019). ITSG-Grace2018: Overview and evaluation of a New GRACE-only gravity field time series. *Journal of Geophysical Research*, *124*(8), 9332–9344. https://doi.org/10.1029/2019JB017415

Lambeck, K., Purcell, A., Zhao, J., & Svensson, N.-O. (2010). The Scandinavian Ice Sheet: From MIS 4 to the end of the Last Glacial Maximum. *Boreas*, *39*(2), 410–435. https://doi.org/10.1111/j.1502-3885.2010.00140.x

Lambeck, K., Rouby, H., Purcell, A., Sun, Y., & Sambridge, M. (2014). Sea level and global ice volumes from the Last Glacial Maximum to the Holocene. *Proceedings of the National Academy of Sciences of the United States of America*, *111*(43), 15296–15303. https://doi.org/10.1073/pnas.1411762111

Larsen, N., Levy, L., Carlson, A., Buizert, C., Olsen, J., Strunk, A., et al. (2018). Instability of the Northeast Greenland Ice Stream over the last 45,000 years. *Nature Communications*, *9*, 1872. https://doi.org/10.1038/s41467-018-04312-7

Le Meur, E., & Huybrechts, P. (1998). Present-day uplift pattern over Greenland from a coupled ice-sheet/visco-elastic bedrock model. *Geophysical Research Letters*, *25*(21), 3951–3954.

Lecavalier, B., Milne, G., Simpson, M., Wake, L., Huybrechts, P., Tarasov, L., et al. (2014). A model of Greenland ice sheet deglaciation constrained by observations of relative sea level and ice extent. *Quaternary Science Reviews*, *102*, 54–84. https://doi.org/10.1016/j.quascirev.2014.07.018

Legrésy, B., Rémy, F., & Blarel, F. (2006). Along track repeat altimetry for ice sheets and continental surface studies(ESA-SP No. 614, paper No. 181). *Proceedings of Symposium on 15 years of progress in radar altimetry, Venice, Italy, 13–18 March 2006*. Noordwijk, The Netherlands: European Space Agency Publication Division.

Ligtenberg, S., Kuipers Munneke, P., Noël, B., & van den Broeke, M. (2018). Brief communication: Improved simulation of the present-day Greenland firn layer (1960-2016). *Cryosphere*, *12*(5), 1643–1649. https://doi.org/10.5194/tc-12-1643-2018

Loomis, B., Rachlin, K., & Luthcke, S. (2019). Improved Earth oblateness rate reveals increased ice sheet losses and mass-driven sea level rise. *Geophysical Research Letters*, *46*(12), 6910–6917. https://doi.org/10.1029/2019GL082929

Luthcke, S., Zwally, H., Abdalati, W., Rowlands, D., Ray, R., Nerem, R., et al. (2006). Recent Greenland ice mass loss by drainage system from satellite gravity observations. *Science*, *314*(5803), 1286–1289. https://doi.org/10.1126/science.1130776

Marzeion, B., Champollion, N., Haeberli, W., Langley, K., Leclercq, P., et al. (2017). Observation-based estimates of global glacier mass change and its contribution to sea-level change. *Surveys in Geophysics*, *38*, 105–130. https://doi.org/10.1007/s10712-016-9394-y

Marzeion, B., Jarosch, A., & Hofer, M. (2012). Past and future sea-level change from the surface mass balance of glaciers. *Cryosphere*, *6*, 1295–1322. https://doi.org/10.5194/tc-6-1295-2012

Mayer-Gürr, T., Behzadpur, S., Ellmer, M., Kvas, A., Klinger, B., Strasser, S., & Zehentner, N. (2018). *ITSG-Grace2018—Monthly, daily and static gravity field solutions from GRACE*. GFZ Data Services. https://doi.org/10.5880/ICGEM.2018.003

Mayer, C., Schaffer, J., Hattermann, T., Floricioiu, D., Krieger, L., Dodd, P., et al. (2018). Large ice loss variability at Nioghalvfjerdsfjorden Glacier, Northeast-Greenland. *Nature Communications*, *9*(1), 2768. https://doi.org/10.1038/s41467-018-05180-x

McMillan, M., Leeson, A., Shepherd, A., Briggs, K., Armitage, T., Hogg, A., et al. (2016). A high-resolution record of Greenland mass balance. *Geophysical Research Letters*, *43*(13), 7002–7010. https://doi.org/10.1002/2016GL069666

McMillan, M., Shepherd, A., Sundal, A., Briggs, K., Muir, A., Ridout, A., et al. (2014). Increased ice losses from Antarctica detected by CryoSat-2. *Geophysical Research Letters*, *41*(11), 3899–3905. https://doi.org/10.1002/2014GL060111

Meredith, M., Sommerkorn, M., Cassotta, S., Derksen, C. A. E., Schuur, E. A. G. (2019). IPCC special report on the ocean and cryosphere in a changing climate (pp. 203–320). Retrieved from https://www.ipcc.ch/srocc/chapter/chapter-3-2/

Mottram, R., Simonsen, B. S., Høyer Svendsen, S., Barletta, V., Sandberg Sørensen, L., Nagler, T., et al. (2019). An integrated view of Greenland Ice Sheet mass changes based on models and satellite observations. *Remote Sensing*, *11*(12), 1407. https://doi.org/10.3390/rs11121407

Mouginot, J., Bjørk, A., Millan, R., Scheuchl, B., & Rignot, E. (2018). Insights on the surge behavior of Storstrømmen and L. Bistrup Bræ, Northeast Greenland, over the last century. *Geophysical Research Letters*, *45*(20), 11197–11211. https://doi.org/10.1029/2018GL079052

Mouginot, J., Rignot, E., Bjørk, A. A., van den Broeke, M., Millan, R., Morlighem, M., et al. (2019). Forty-six years of Greenland Ice Sheet mass balance from 1972 to 2018. *Proceedings of the National Academy of Sciences of the United States of America*, *116*(19), 9239–9244. https://doi.org/10.1073/pnas.1904242116

Mouginot, J., Rignot, E., Scheuchl, B., Fenty, I., Khazendar, A., Morlighem, M., et al. (2015). Fast retreat of Zachariæ Isstrøm, northeast Greenland. *Science*, *350*(6266), 1357–1361. https://doi.org/10.1126/science.aac7111

Nagler, T., Rott, H., Hetzenecker, M., Wuite, J., & Potin, P. (2015). The Sentinel-1 Mission: New opportunities for ice sheet observations. *Remote Sensing*, *7*(7), 9371–9389. https://doi.org/10.3390/rs70709371

Noël, B., van de Berg, W., Lhermitte, S., & van den Broeke, M. (2019). Rapid ablation zone expansion amplifies north Greenland mass loss. *Science Advances*, *5*(9), eaaw0123. https://doi.org/10.1126/sciadv.aaw0123

Noël, B., van de Berg, W., Lhermitte, S., Wouters, B., Machguth, H., Howat, I., et al. (2017). A tipping point in refreezing accelerates mass loss of Greenland's glaciers and ice caps. *Nature Communications*, *8*, 14730. https://doi.org/10.1038/ncomms14730

Noël, B., van de Berg, W., Machguth, H., Lhermitte, S., Howat, I., Fettweis, X., & van den Broeke, M. (2016). A daily, 1 km resolution data set of downscaled Greenland ice sheet surface mass balance (1958–2015). *Cryosphere*, *10*(5), 2361–2377. https://doi.org/10.5194/tc-10-2361-2016

Noël, B., van de Berg, W., van Wessem, J., van Meijgaard, E., van As, D., Lenaerts, J., et al. (2018). Modeling the climate and surface mass balance of polar ice sheets using RACMO2—Part 1: Greenland (1958–2016). *Cryosphere*, *12*(3), 811–831. https://doi.org/10.5194/tc-12-811-2018

Peltier, W. (2004). Global glacial isostasy and the surface of the ice-age Earth: The ICE-5G (VM2) model and GRACE. *Annual Review of Earth and Planetary Sciences*, *32*(1), 111–149. https://doi.org/10.1146/annurev.earth.32.082503.144359

Peltier, W., Argus, D., & Drummond, R. (2015). Space geodesy constrains ice age terminal deglaciation: The global ICE-6G_C (VM5a) model: Global Glacial Isostatic Adjustment. *Journal of Geophysical Research*, *120*(1), 450–487. https://doi.org/10.1002/2014JB011176

Peltier, W., Argus, D., & Drummond, R. (2018). Comment on "An Assessment of the ICE-6G_C (VM5a) Glacial Isostatic Adjustment Model" by Purcell et al. *Journal of Geophysical Research*, *123*(2), 2019–2028. https://doi.org/10.1002/2016JB013844

Petit, G., & Luzum, B. (Eds.). (2010). *IERS conventions (2010) (IERS Technical Note; No. 36)*. Frankfurt am Main, Germany: Verlag des Bundesamts für Kartographie und Geodäsie. Retrieved from http://www.iers.org/nn%5Ctext%7B%5C%5F%7D11216/IERS/EN/Publications/TechnicalNotes/tn36.html

Porter, C., Morin, P., Howat, I., Noh, M.-J., Bates, B., Peterman, K., et al. (2018). ArcticDEM, . *Harvard Dataverse*, https://doi.org/10.7910/DVN/OHHUKH

Ray, R., & Luthcke, S. (2006). Tide model errors and GRACE gravimetry: toward a more realistic assessment. *Geophysical Journal International*, *167*(3), 1055–1059. https://doi.org/10.1111/j.1365-246X.2006.03229.x

Rebischung, P., Altamimi, Z., Ray, J., & Garayt, B. (2016). The IGS contribution to ITRF2014. *Journal of Geodynamics*, *90*(7), 611–630. https://doi.org/10.1007/s00190-016-0897-6

RGI Consortium (2017). *Randolph glacier inventory—A dataset of global glacier outlines: Version 6.0. Technical report, Global Land Ice Measurements from Space*. CO, USA. https://doi.org/10.7265/N5-RGI-60

Rignot, E., & Mouginot, J. (2012). Ice flow in Greenland for the International Polar Year 2008–2009. *Geophysical Research Letters*, *39*(11), L11501. https://doi.org/10.1029/2012GL051634

Rignot, E., Velicogna, I., van den Broeke, M., Monaghan, A., & Lenaerts, J. (2011). Acceleration of the contribution of the Greenland and Antarctic ice sheets to sea level rise. *Geophysical Research Letters*, *38*(5), L05503. https://doi.org/10.1029/2011GL046583

Rinne, E., Shepherd, A., Palmer, S., van den Broeke, M., Muir, A., Ettema, J., & Wingham, D. (2011). On the recent elevation changes at the Flade Isblink Ice Cap, northern Greenland. *Journal of Geophysical Research*, *116*(F03024), 1–9. https://doi.org/10.1029/2011JF001972

Rülke, A. (2009). *Zur Realisierung eines terrestrischen Referenzsystems in globalen und regionalen GPS-Netzen (Doctoral dissertation, Technische Universität Dresden)*. Retrieved from http://nbn-resolving.de/urn:nbn:de:bsz:14-qucosa-24543(188S

Sandberg Sørensen, L., Simonsen, S., Forsberg, R., Khvorostovsky, K., Meister, R., & Engdahl, M. (2018). 25 years of elevation changes of the Greenland Ice Sheet from ERS, Envisat, and CryoSat-2 radar altimetry. *Earth and Planetary Science Letters*, *495*, 234–241. https://doi.org/10.1016/j.epsl.2018.05.015

Sasgen, I., Konrad, H., Helm, V., & Grosfeld, K. (2019). High-resolution mass trends of the Antarctic Ice Sheet through a spectral combination of satellite gravimetry and radar altimetry observations. *Remote Sensing*, *11*(2), 144. https://doi.org/10.3390/rs11020144

Schaffer, J., Kanzow, T., von Appen, W.-J., von Albedyll, L., Arndt, J., & Roberts, D. (2020). Bathymetry constrains ocean heat supply to Greenland's largest glacier tongue. *Nature Geoscience*, *13*, 227–231. https://doi.org/10.1038/s41561-019-0529-x

Schaffer, J., von Appen, W.-J., Dodd, P., Hofstede, C., Mayer, C., de Steur, L., & Kanzow, T. (2017). Warm water pathways toward Nioghalvfjerdsfjorden Glacier, Northeast Greenland. *Journal of Geophysical Research*, *122*(5), 4004–4020. https://doi.org/10.1002/2016JC012462

Schrama, E., Wouters, B., & Rietbroek, R. (2014). A mascon approach to assess ice sheet and glacier mass balances and their uncertainties from GRACE data. *Journal of Geophysical Research*, *119*(7), 6048–6066. https://doi.org/10.1002/2013JB010923

Schröder, L., Horwath, M., Dietrich, R., Helm, V., van den Broeke, M., & Ligtenberg, S. (2019). Four decades of Antarctic surface elevation changes from multi-mission satellite altimetry. *Cryosphere*, *13*(2), 427–449. https://doi.org/10.5194/tc-13-427-2019

Shepherd, A., Ivins, E., Rignot, E., Smith, B., van den Broeke, M., Velicogna, I., et al. (2019). Mass balance of the Greenland Ice Sheet from 1992 to 2018. *Nature*, *579*, 233–239. https://doi.org/10.1038/s41586-019-1855-2

Simonsen, S., & Sørensen, L. (2017). Implications of changing scattering properties on Greenland ice sheet volume change from Cryosat-2 altimetry. *Remote Sensing of Environment*, *190*, 207–216. https://doi.org/10.1016/j.rse.2016.12.012

Simpson, M., Milne, G., Huybrechts, P., & Long, A. (2009). Calibrating a glaciological model of the Greenland ice sheet from the Last Glacial Maximum to present-day using field observations of relative sea level and ice extent. *Quaternary Science Reviews*, *28*(17–18), 1631–1657. https://doi.org/10.1016/j.quascirev.2009.03.004

Sørensen, L., Simonsen, S., Nielsen, K., Lucas-Picher, P., Spada, G., Adalgeirsdottir, G., et al. (2011). Mass balance of the Greenland ice sheet (2003–2008) from ICESat data—The impact of interpolation, sampling and firn density. *Cryosphere*, *5*(1), 173–186. https://doi.org/10.5194/tc-5-173-2011

Strößenreuther, U., Horwath, M., & Schröder, L. (2020). How different analysis and interpolation methods affect the accuracy of ice surface elevation changes inferred from satellite altimetry. *Mathematical Geosciences*, *52*, 499–525. https://doi.org/10.1007/s11004-019-09851-3

Strunk, A., Larsen, N., Nilsson, A., Seidenkrantz, M., Levy, L., Olsen, J., & Lauridsen, T. (2018). Relative sea-level changes and ice sheet history in Finderup Land, North Greenland. *Frontiers of Earth Science*, *6*, 129. https://doi.org/10.3389/feart.2018.00129

Sun, Y., Riva, R., & Ditmar, P. (2016). Optimizing estimates of annual variations and trends in geocenter motion and J_2 from a combination of GRACE data and geophysical models. *Journal of Geophysical Research*, *121*(11), 8352–8370. https://doi.org/10.1002/2016JB013073

Swenson, S., Chambers, D., & Wahr, J. (2008). Estimating geocenter variations from a combination of GRACE and ocean model output. *Journal of Geophysical Research*, *113*, B08410. https://doi.org/10.1029/2007JB005338

Swenson, S., & Wahr, J. (2002). Methods for inferring regional surface-mass anomalies from Gravity Recovery and Climate Experiment (GRACE) measurements of time-variable gravity. *Journal of Geophysical Research*, *107*(B9), 2193. https://doi.org/10.1029/2001JB000576

Tanaka, Y., Klemann, V., Martinec, Z., & Riva, R. (2011). Spectral-finite element approach to viscoelastic relaxation in a spherical compressible Earth: Application to GIA modeling. *Geophysical Journal International*, *184*(1), 220–234. https://doi.org/10.1111/j.1365-246X.2010.04854.x

Tarasov, L., Dyke, A., Neal, R., & Peltier, W. (2012). A data-calibrated distribution of deglacial chronologies for the North American ice complex from glaciological modeling. *Earth and Planetary Science Letters*, *315–316*, 30–40. https://doi.org/10.1016/j.epsl.2011.09.010

Tarasov, L., & Peltier, W. (2002). Greenland glacial history and local geodynamic consequences. *Geophysical Journal International*, *150*(1), 198–229. https://doi.org/10.1046/j.1365-246X.2002.01702.x

Thomas, R., Davis, C., Frederick, E., Krabill, W., Li, Y., Manizade, S., & Martin, C. (2008). A comparison of Greenland ice-sheet volume changes derived from altimetry measurements. *Journal of Glaciology*, *54*(185), 203–212. https://doi.org/10.3189/002214308784886225

van Dam, T., Wahr, J., & Lavallée, D. (2007). A comparison of annual vertical crustal displacements from GPS and Gravity Recovery and Climate Experiment (GRACE) over Europe. *Journal of Geophysical Research*, *112*, B03404. https://doi.org/10.1029/2006JB004335

van den Broeke, M., Bamber, J., Ettema, J., Rignot, E., Schrama, E., van de Berg, W., et al. (2009). Partitioning recent Greenland mass loss. *Science*, *326*(5955), 984–986. https://doi.org/10.1126/science.1178176

Wagner, B., & Bennike, O. (2014). Holocene environmental change in the Skallingen area, eastern North Greenland, based on a lacustrine record: Holocene environmental change, eastern N Greenland. *Boreas*, *44*(1), 45–59. https://doi.org/10.1111/bor.12085

Wahr, J., Molenaar, M., & Bryan, F. (1998). Time variability of the Earth's gravity field: Hydrological and oceanic effects and their possible detection using GRACE. *Journal of Geophysical Research*, *103*(B12), 30205–30229. https://doi.org/10.1029/98JB02844

Wahr, J., Wingham, D., & Bentley, C. (2000). A method of combining ICESat and GRACE satellite data to constrain Antarctic mass balance. *Journal of Geophysical Research*, *105*(B7), 16279–16294. https://doi.org/10.1029/2000JB900113

Wake, L., Lecavalier, B., & Bevis, M. (2016). Glacial Isostatic Adjustment (GIA) in Greenland: A Review. *Current Climate Change Reports*, *2*(3), 101–111. https://doi.org/10.1007/s40641-016-0040-z

Wang, L., Khan, S., Bevis, M., van den Broeke, M., Kaban, M., Thomas, M., & Chen, C. (2019). Downscaling GRACE predictions of the crustal response to the present-day mass changes in Greenland. *Journal of Geophysical Research*, *124*(5), 5134–5152. https://doi.org/10.1029/2018JB016883

Wang, H., Xiang, L., Jia, L., Jiang, L., Wang, Z., Hu, B., & Gao, P. (2012). Load Love numbers and Green's functions for elastic Earth models PREM, iasp91, ak135, and modified models with refined crustal structure from Crust 2.0. *Computers & Geosciences*, *49*, 190–199. https://doi.org/10.1016/j.cageo.2012.06.022

WCRP Global Sea Level Budget Group (2018). Global sea level budget 1993–Present. *Earth System Science Data*, *10*(3), 1551–1590. https://doi.org/10.5194/essd-10-1551-2018

Weidick, A. (1995). Satellite image atlas of glaciers of the world–Greenland (pp. *C64–C67)*. U. S. Geological Survey.

Weidick, A., Andreasen, C., Oerter, H., & Reeh, N. (1996). Neoglacial glacier changes around Storstrømmen, North-East Greenland. *Polarforschung*, *64*(3), 95–108.

Williams, S. (2003). The effect of colored noise on the uncertainties of rates estimated from geodetic time series. *Journal of Geodynamics*, *76*, 483–494. https://doi.org/10.1007/s00190-002-0283-4

Williams, S. (2008). CATS: GPS coordinate time series analysis software. *GPS Solutions*, *12*(2), 147–153. https://doi.org/10.1007/s10291-007-0086-4

Wingham, D., Francis, C., Baker, S., Bouzinac, C., Brockley, D., Cullen, R., et al. (2006). CryoSat: A mission to determine the fluctuations in Earth's land and marine ice fields. *Advances in Space Research*, *37*, 841–871. https://doi.org/10.1016/j.asr.2005.07.027

Wouters, B., Chambers, D., & Schrama, E. (2008). GRACE observes small-scale mass loss in Greenland. *Geophysical Research Letters*, *35*, L20501. https://doi.org/10.1029/2008GL034816

Wouters, B., Martín-Español, A., Helm, V., Flament, T., van Wessem, J., Ligtenberg, S., et al. (2015). Dynamic thinning of glaciers on the Southern Antarctic Peninsula. *Science*, *348*(6237), 899–903. https://doi.org/10.1126/science.aaa5727

Zemp, M., Huss, M., Thibert, E., Eckert, N., McNabb, R., Huber, J., et al. (2019). Global glacier mass changes and their contributions to sea-level rise from 1961 to 2016. *Nature*, *568*, 382–386. https://doi.org/10.1038/s41586-019-1071-0